TECHNISCHE UNIVERSITÄT WIEN

DIPLOMARBEIT

Performance enhancement in multi-wavelength systems using vertical-cavity surface-emitting lasers

ausgeführt am Institut für
Nachrichtentechnik und Hochfrequenztechnik der
Technischen Universität Wien
von

Christian Hambeck

Reschstraße 12
3385 Gerersdorf

Matrikelnummer 0125153

Wien, im November 2006

Betreuer:

DI. Franz Fidler
Prof. Dr. Walter R. Leeb

This work was partly sponsored by HOCHSCHULJUBILÄUMSSTIFTUNG DER STADT WIEN.

Danksagung

Ich möchte mich bei allen bedanken, die mit ihrer fachlichen und persönlichen Unterstützung zum Gelingen dieser Diplomarbeit beigetragen haben.

Ich danke meinen Eltern, Herta und Johann Hambeck, die mir das Studium der Elektrotechnik ermöglicht haben.

Herzlichen Dank auch an Prof. Dr. Walter Leeb, Vorstand des Instituts für Nachrichten- und Hochfrequenztechnik, für die zahlreichen Anregungen und für die Unterstützung bei der Anschaffung von Ausrüstung für diese Diplomarbeit.

Ganz besonders möchte ich mich bei Herrn DI Franz Fidler bedanken, für die ausgezeichnete Betreuung, die zahlreichen aufschlussreichen Diskussionen und Ratschläge, sowie für seine kollegiale Unterstützung, sowohl bei der Bewältigung von technischen Problemen, vor allem aber auch für die Hilfe bei organisatorischen Anliegen während der Durchführung dieser Diplomarbeit.

Ich danke meinen Geschwistern Birgit und Melanie Hambeck, sowie allen lieben Freunden und Studienkollegen, die mich während meines Studiums immer unterstützt haben.

Christian Hambeck

Kurzfassung

In optischen Kommunikationssystemen spielen die eingesetzten Laserquellen eine wichtige Rolle. Durch Fortschritte in der Halbleitertechnologie ist es gelungen, vertikal emittierende Laser (VCSELs) im Wellenlängenbereich um 1.55 μm herzustellen, welche im Gegensatz zu kanten-emittierenden Lasern zahlreiche Vorteile, wie etwa geringen Leistungsverbrauch oder das Potential für kostengünstige Massenproduktion, bieten.
In meiner Arbeit werden zwei Einsatzgebiete für solche neuartigen, langwelligen VCSELs behandelt. Im ersten Teil befasse ich mich mit der Leistungssteigerung in Glasfaser-gebundenen Wellenlängenmultiplex-Systemen. Im zweiten Teil der Diplomarbeit untersuche ich die Technik der Wellenlängendiversität, als eine Möglichkeit zur Kompensation der Auswirkungen von atmosphärischer Turbulenz in der Freistrahlkommunikation.

Durch das stetige Wachstum des Internets und immer neuerer Kommunikationsanwendungen, ist es erforderlich, laufend innovative Technologien einzusetzen, damit der steigende Bandbreitenbedarf gedeckt werden kann. In optischen Wellenlängenmultiplex (WDM)-Systemen werden dazu mehrere Informationskanäle durch Signale bei unterschiedlichen Wellenlängen über eine gemeinsame Glasfaser übertragen. Ziel aktueller Forschungsprojekte ist es, neben der Steigerung der überbrückbaren Distanzen und der Erhöhung der Übertragungskapazitäten, eine Kostenreduktion von WDM-Systemen zu erreichen, um auch im Netzzugangsbereich eine optische Breitbandanbindung ermöglichen zu können.
In meiner Arbeit präsentiere ich ein bidirektioanales 4-Kanal-WDM-System mit einem Kanalabstand von 20 nm (CWDM), welches eine ökonomische Realisierung durch den Einsatz von kostengünstigen und kommerziell erhältlichen Komponenten erlaubt. Im experimentellen CWDM-System werden nicht selektierte, ungekühlte und direkt modulierte VCSELs im Wellenlängenbereich von 1531 nm bis 1591 nm verwendet, die für einen Betrieb mit 2.5 Gb/s spezifiziert sind, jedoch mit einer Datenrate von 10.7 Gb/s betrieben werden. Ermöglicht wird dies durch eine von mir entworfene Hochfrequenz-Schaltung, welche die Bandbreitenlimitierung des Lasergehäuses von 4 GHz auf 10 GHz anhebt. In Kombination mit fehlerkorrigierender Kodierung (FEC) führt das Zusammenwirken des Laserchirps mit der Dispersion auf der Standard-Glasfaser zu Übertragungsdistanzen des CWDM-Systems von mehr als 45 km. Ich habe gezeigt, dass diese leistungsbegrenzte Reichweite durch den Einsatz von VCSELs mit höherer Ausgangsleistung auf eine dispersionsbegrenzte Distanz von bis zu 77 km ausgeweitet werden kann.

Ein weiteres Anwendungsgebiet von langwelligen VCSELs ist die optische Freistrahlkommunikation. Die Ausbreitung des Laserstrahls durch turbulente Luftströmungen in der Atmosphäre führt jedoch zu Leistungsschwankungen am Empfänger. Eine Möglichkeit, diese Auswirkungen der Turbulenz zu kompensieren, ist Wellenlängendiversität.
In meiner Arbeit verwende ich VCSEL mit zwei unterschiedlichen Wellenlängen, um die Statistik der empfangsseitig auftretenden Intensitätsschwankungen zu verbessern. Die Ergebnisse meiner Experimente zeigen, dass die Wellenlängenabhängigkeit der atmosphärischen Turbulenz sehr gering ausgeprägt ist, was zu einem verminderten Nutzen dieses Prinzips für praktische Anwendungen führt.

Abstract

In optical communication systems, the choice of the laser sources is very important. Due to advances in semiconductor technology, it is possible to fabricate *vertical-cavity surface-emitting lasers* (VCSELs) at long wavelengths around 1.55 μm. They offer numerous advantages in comparison to edge-emitting lasers like low power consumption, and the potential for low cost and high volume mass production.
In my work, I discuss two fields of applications for such novel long wavelength VCSELs. In the first part, I deal with performance enhancement in fiber-based *wavelength division multiplexing* (WDM) systems. In the second part of my thesis, I analyze the technique of wavelength diversity as one possibility to compensate the impact of atmospheric turbulence in optical free-space communication.

Due to the steady expansion of the Internet, innovative technologies will have to be employed to satisfy the increasing demand on bandwidth associated with new communications services. Optical WDM systems use signals at different wavelengths for each data channel, which are transmitted over one common fiber. The aim of recent research activities is – beside an improvement of reachable distance and capacity – a reduction of the costs of such systems in order to enable the use of broadband connections also in access networks.
In my thesis, I present a bidirectional 4-channel-WDM-system with a channel spacing of 20 nm (CWDM), which allows for economic realization via the use of commercial available, low cost components. In the experimental CWDM system, non-selected, uncooled, and directly modulated VCSELs in the wavelength range from 1531 nm to 1591 nm are utilized, which are rated for 2.5 Gb/s, but driven at a data rate of 10.7 Gb/s. This is made possible by the use of a proprietary developed radio-frequency-schematic, which increases the bandwidth limitation of the VCSELs' packages from 4 GHz to 10 GHz. In combination with forward error correction (FEC), the interplay between laser chirp and dispersion on the standard single-mode fiber leads to a maximum transmission distance of the CWDM system of more than 45 km. I have shown, that this power-limited reach can be extended up to a dispersion-limited distance of 77 km via the use of VCSELs with higher output power.

Another application of long wavelength VCSELs is optical free-space communication. The propagation of the laser beam through turbulent air in the atmosphere causes power fluctuations at the receiver. A possibility to compensate this impact of turbulence, is wavelength diversity.
In my work, I use VCSELs at two different wavelengths to improve the statistics of the intensity variations at the receiver. However, the results of my experiments show that the wavelength dependency of the atmospheric turbulence is very low. This leads to a reduced benefit of this principle for practical applications.

Contents

Part I

Fiber-based wavelength division multiplexing (WDM) systems

Chapter 1

CWDM transmission systems

Data traffic over the internet increases rapidly and doubles approximately every 6 to 12 months [1]. Because of an increasing demand of broadband applications, optical access networks become more and more important. These systems should offer the advantage of high data rates per channel as well as reduction of the cost per transmitted bit. One way to achieve this, is to use the technique of *coarse wavelength division multiplexing* (CWDM).

A point-to-point WDM link is shown in Fig. 1.1. Multiple channels or wavelengths are transmitted over one common fiber. In a system with N channels at bit rates R_1 to R_N, the total bit rate R_{agg} becomes

$$R_{agg} = R_1 + R_2 + ... + R_N. \tag{1.1}$$

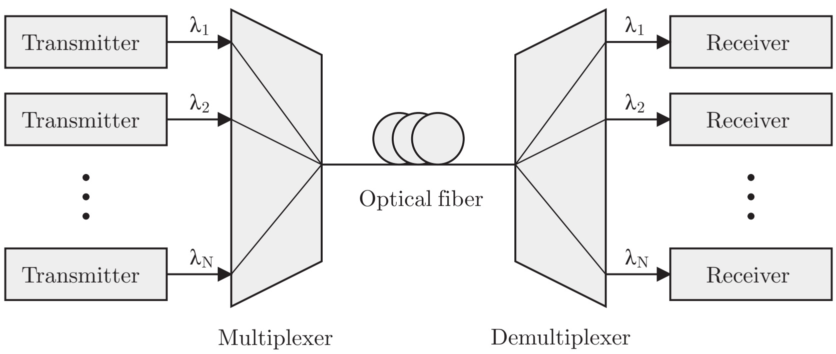

Figure 1.1: Wavelength division multiplexing point-to-point fiber link.

Coarse wavelength division multiplexing systems use center wavelengths from 1271 to 1611 nm (cf. Fig. 1.2) and they have a relatively wide channel spacing of 20 nm [2] compared to *dense wavelength division multiplexing* (DWDM) systems [3], which are mainly used in long-haul networks. Non thermic stabilized semiconductor laser sources like *distributed feedback* (DFB) lasers or *vertical cavity surface emitting lasers* (VCSELs) in combination with optical thin film multiplexers can be used.
The main advantage of CWDM systems are lower costs of the used components and a reduced system complexity.

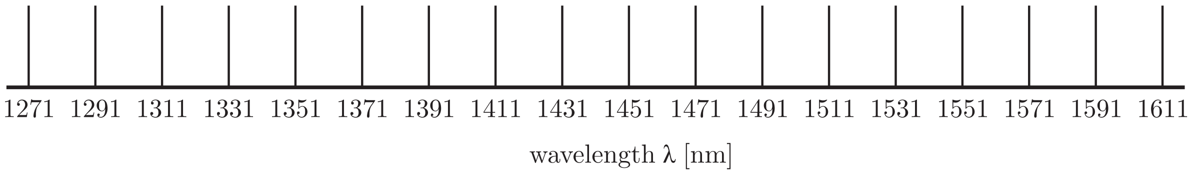

Figure 1.2: 18 channel CWDM grid of the ITU-T G.695 standard [4].

The main applications of CWDM systems are in short-reach access networks, like *local area networks* (LANs) and *access passive optical networks* (PONs) like *"fiber to the business"* (FTTB), *"fiber to the curb"* (FTTC) or *"fiber to the home"* (FTTH). Using commercial available components like DFB-lasers, VCSELs, thin film multiplexers, *standard single mode fibers* (SSMFs), and pin-receivers, it is possible to build an economic passive optical network at data rates of up to 10 Gb/s [5]. In actual research efforts, equalization and forward error correction is used to enhance the performance of such systems [6, 7].

In this work, I demonstrate a 4-channel CWDM transmission over standard single mode fiber using commercially available vertical cavity surface emitting lasers that cover the CWDM band from 1531 to 1591 nm, operating at a data rate of 10.7 Gb/s. This bit rate allows for enhanced *forward error correction* (FEC), but I did not use any kind of dispersion compensation.

Chapter 2

Components of the CWDM transmission system

In the following chapter, the main components of my CWDM experiments are described and characterized. Figure 2.1 schematically gives an overview of the necessary components in a bidirectional 4-channel CWDM system at a per-channel data rate of 10.7 Gb/s.

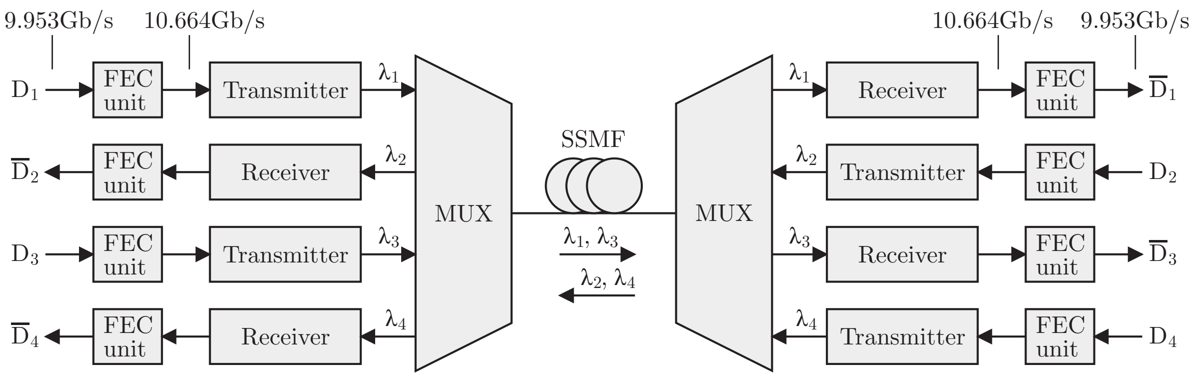

Figure 2.1: Main components of the CWDM system.

As transmission sources, I used uncooled *directly modulated* VCSELs. The different wavelengths are multiplexed via thin-film multiplexers onto a SSMF and transmitted without amplification. After demultiplexing, a pin-receiver converts the optical signal to the electrical domain. The wavelengths from 1531 nm to 1591 nm are used to transmit four independent data streams (cf. Table 2.1).

channel	wavelength λ [nm]
1	1531
2	1551
3	1571
4	1591

Table 2.1: Channel grid of the CWDM system.

To enhance the span of the system, a *forward error correction* (FEC) unit can be used, also in order to combat in-band crosstalk caused by multiplexers and Rayleigh backscattering. Therefore, the per channel data rate $R_{SON} = 9.95328\,\text{Gb/s}$ in the case of SONET has to be increased by a 7 % overhead to $R = 10.664\,\text{Gb/s}$ (cf. Section 2.1).

2.1 Forward error correction (FEC)

Forward error correction uses coding to improve the transmission quality. The ITU has standardized a 7 % overhead to guarantee interoperability [8, 9]. FEC devices are able to correct single bit errors. Burst-errors can only be corrected to a certain length.

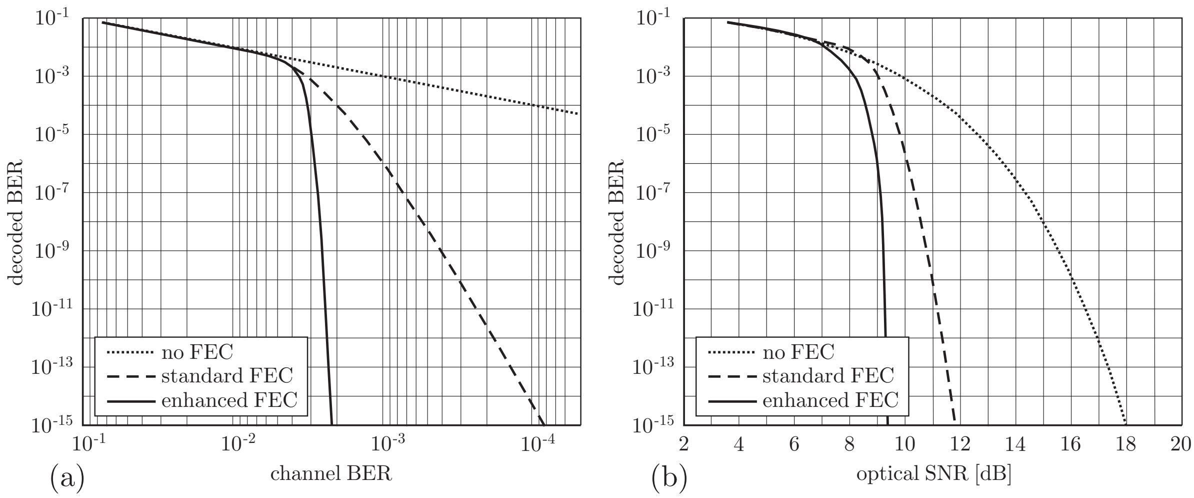

Figure 2.2: Performance of standard FEC and enhanced FEC [8, 9, 10].

Figure 2.2 compares the performance of *standard* FEC (SFEC) using a Reed-Solomon code RS(255,239) to *enhanced* FEC (EFEC). EFEC is able to correct *bit error ratios* (BERs) from $2 \cdot 10^{-3}$ to values below 10^{-15}. For noise limited systems with a specified BER of 10^{-12}, Fig. 2.2(b) shows an additional 7.7 dB gain compared to a system without FEC.
Manufacturers of FEC devices for data rates of up to 10 Gb/s are for example Intel, Agere, AMCC, or Vitesse.

2.2 Transmitter

The key issues in optical access networks are the reduction of cost and power consumption. To fulfil these requirements directly modulated long wavelength VCSELs can be used. Compared to DFB-lasers, VCSELs have the potential for high volume mass production and on chip testing, which may reduce the cost of these laser sources in the near future.

2.2.1 Directly modulated VCSELs

To demonstrate 4-channel high-speed CWDM transmission, I used four single-mode pigtailed, uncooled VCSELs from Vertilas, rated for 2.5 Gb/s, but driven at a data rate of 10.7 Gb/s with *non-return-to-zero* (NRZ) modulation. This was made possible by mounting the VCSELs at the end of a 50 Ω microstrip line, in series with an RC element, as shown in Fig. 2.3(a).

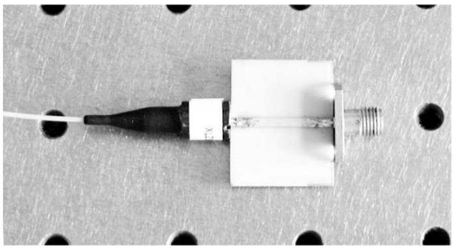

(a)

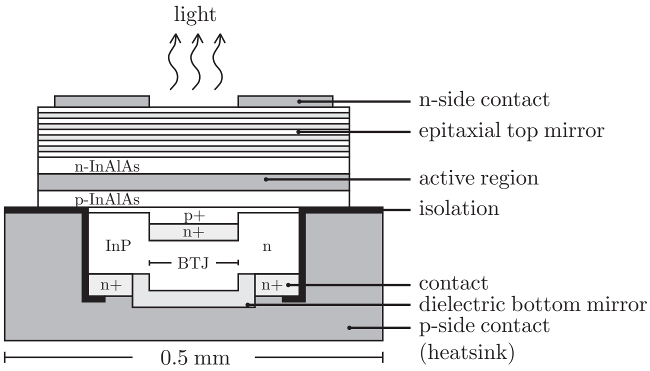

(b)

Figure 2.3: (a) VCSEL mounted on 50 Ω microstrip line, (b) layering of Vertilas' VCSELs [11].

Figure 2.3(b) shows the functional layering of the VCSEL. The symmetric aperture causes a circular *full with half maximum* (FWHM) beam divergence of 20 degree and allows efficient coupling into a single-mode fiber.

2.2.2 Static characteristics of VCSELs

The VCSELs were not preselected and thus had widely varying static as well as dynamic characteristics. Figure 2.4 shows the measurement setup for the static characterization of the VCSELs.

Measurement setup for static characteristics

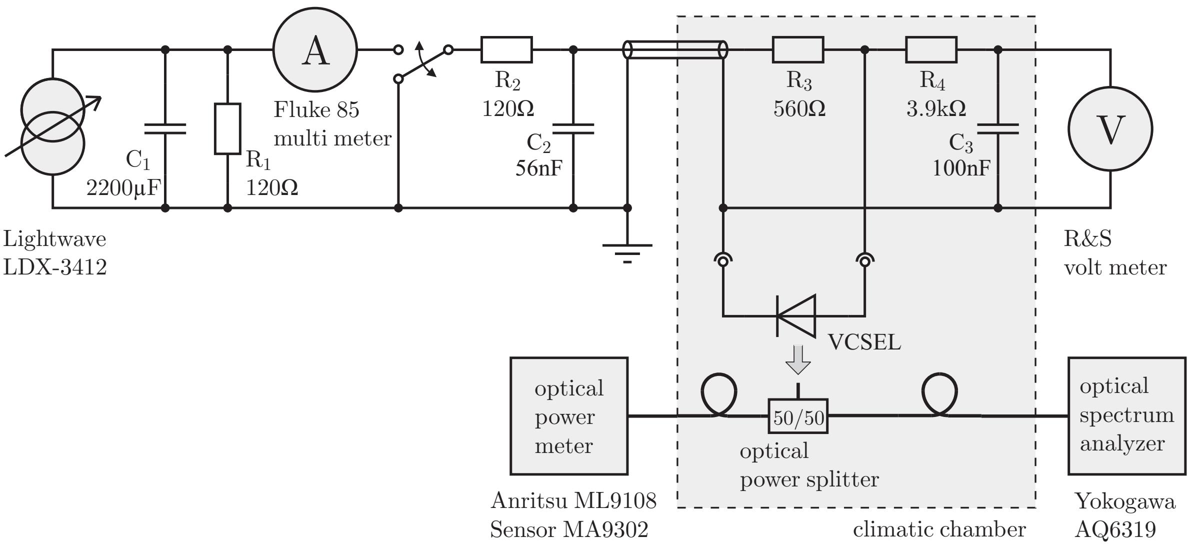

Figure 2.4: Measurement setup for static characterization of VCSELs.

The VCSELs are very sensitive to *electrostatic discharge* (ESD). Therefore, a carefully designed measurement setup for ESD and surge protection is necessary as well as grounding the human body of the operator.

The low pass filter after the current source consisting of R_1 and C_1 has a long time constant of $\tau_1 = R_1 \cdot C_1 = 0.26\,\mathrm{s}$, and absorbs surges caused by the current source due to voltage variation on the power line. R_2 and C_2 protect the VCSEL from transients of the switch, which is used to disconnect the laser from the source for grounding the VCSEL. The volt meter produces a small voltage ripple on its inputs. Therefore, the foil capacitor C_3 is used to shorten it, and R_4 decouples the remaining ripple from the laser. Its value is chosen small enough not to influence the voltage measurement accuracy of the volt meter. Finally, R_3 is designed to limit the maximum source current to the absolute maximum rating of the laser.

Static results for 1531 nm VCSEL

Figure 2.5(a) shows the voltage vs. current (U-I) characteristics and the power vs. current (P-I) characteristics of the 1531 nm VCSEL for various ambient temperatures from 25 to 50 °C.

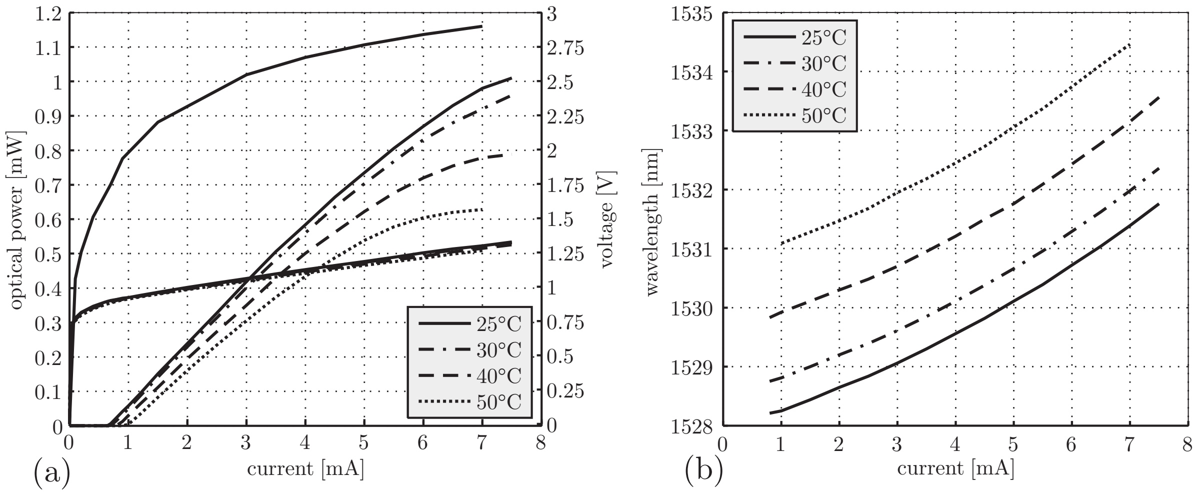

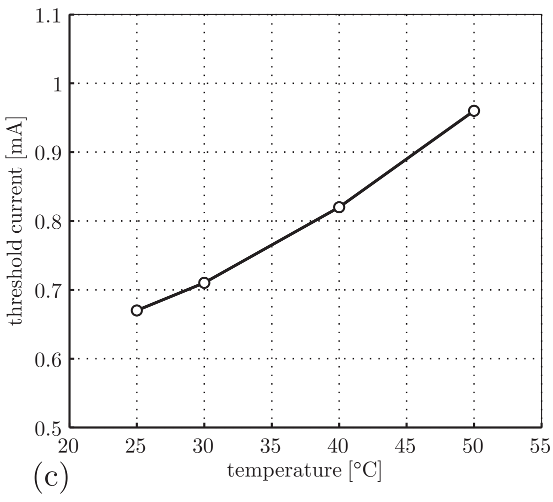

ambient temperature T_a [°C]	slope efficiency E_s [W/A]	differential resistance R_d [Ω]
25	0.181	68
30	0.177	66
40	0.162	64
50	0.157	62

(d)

Figure 2.5: Static characteristics at various temperatures of the 1531 nm VCSEL.

Higher temperatures lead to a reduction of the output power, which partially was an effect of additional coupling loss into the single-mode fiber. After cooling down the laser, it doubled its forward voltage. The other characteristics didn't change apart from a slightly slower optical output power due to increased power dissipation. The original laser cavity seemed to operate normal, only the intrinsic electrical characteristic changed. Figure 2.5(b) shows the temperature dependence of the laser's wavelength, mainly caused by thermal expansion of the laser cavity, which is about 0.116 nm/K. Part (c) of Fig. 2.5 describes the increasing threshold current with temperature, whereas the table in Fig. 2.5(d) lists slope efficiencies and differential resistances for a constant bias current of 5 mA.

Static results for 1551 nm VCSEL

Figure 2.6 shows the DC-characteristics of the 1551 nm VCSEL at various ambient temperatures from 25 °C to 40 °C.

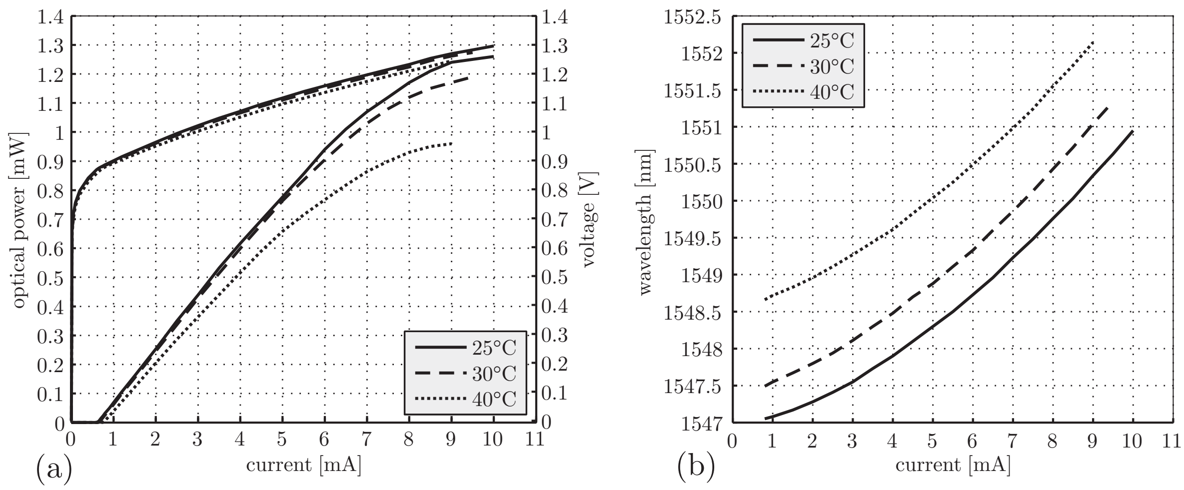

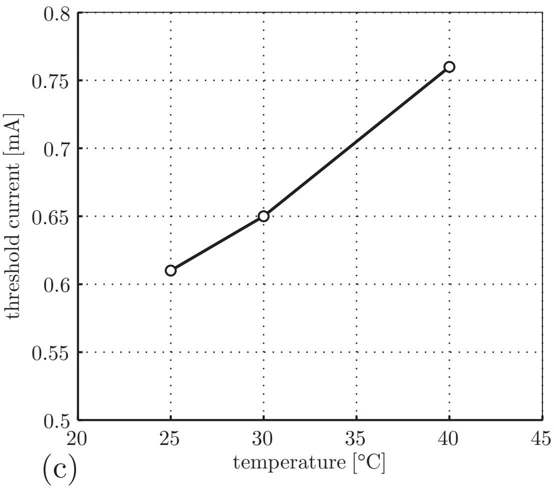

ambient temperature T_a [°C]	slope efficiency E_s [W/A]	differential resistance R_d [Ω]
25	0.182	52
30	0.181	52
40	0.164	51

(d)

Figure 2.6: Static characteristics at various temperatures of the 1551 nm VCSEL: (a) P-I and U-I characteristics, (b) wavelength vs. laser current, (c) threshold current vs. temperature, and (d) slope efficiency and differential resistance as a function of ambient temperature.

The maximum temperature had been reduced compared to the 1531 nm VCSEL to protect the laser and its coupling to the fiber from nonreversible thermal effects. The wavelength dependence of this laser is about 0.113 nm/K and the differential resistance of approximately 52 Ω was determined at a bias current of 7 mA.

Static results for 1571 nm VCSEL

Figure 2.7 shows the DC-characteristics of the 1571 nm VCSEL in the ambient temperature range from 25 °C to 40 °C. The wavelength dependence of the laser is about 0.115 nm/K and its differential resistance of approximately 57 Ω was measured at a bias current of 7 mA.

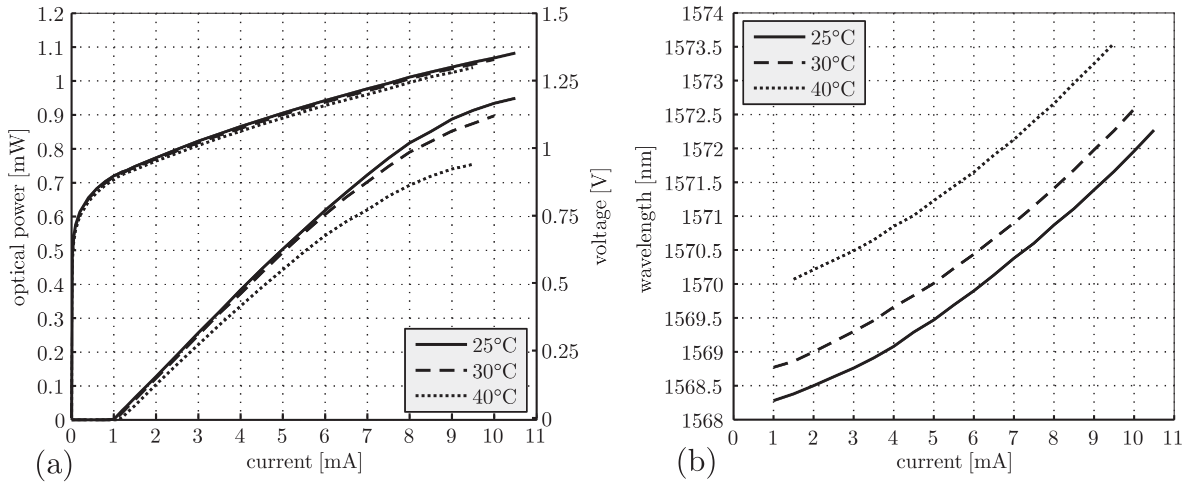

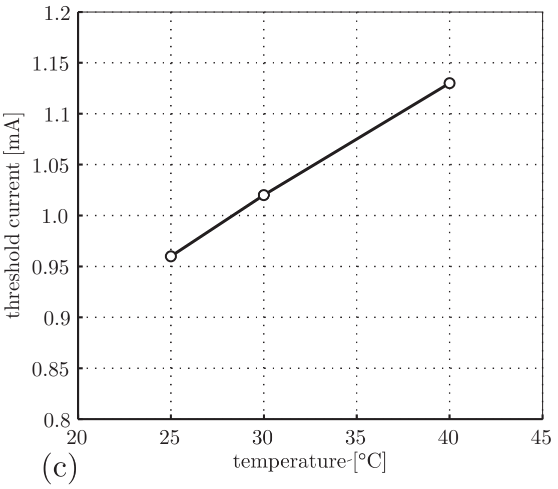

ambient temperature T_a [°C]	slope efficiency E_s [W/A]	differential resistance R_d [Ω]
25	0.128	58
30	0.127	57
40	0.120	56

(d)

Figure 2.7: Static characteristics at various temperatures of the 1571 nm VCSEL: (a) P-I and U-I characteristics, (b) wavelength vs. laser current, (c) threshold current vs. temperature, and (d) slope efficiency and differential resistance as a function of ambient temperature.

Static results for 1591 nm VCSEL

Figure 2.8 shows the DC-characteristics of the 1591 nm VCSEL in the ambient temperature range from 25 °C to 40 °C. This laser had the lowest output power in the CWDM system of maximal 0.9 mW. The threshold current at 25 °C is significantly higher compared to the other VCSELs and it decreases slightly with temperature. The laser's wavelength dependence was measured to be 0.119 nm/K and its differential resistance of approximately 53 Ω was determined at a bias current of 7 mA.

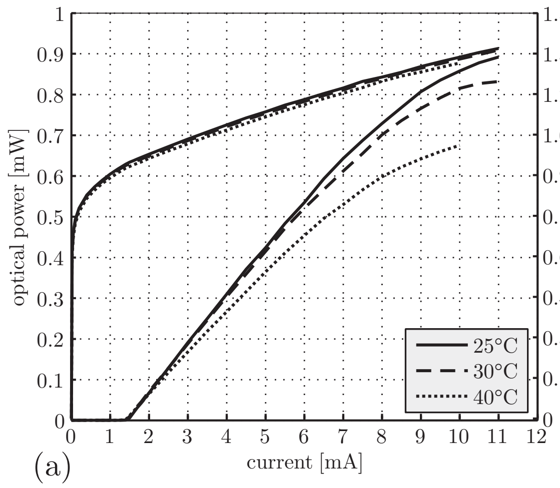

(a)

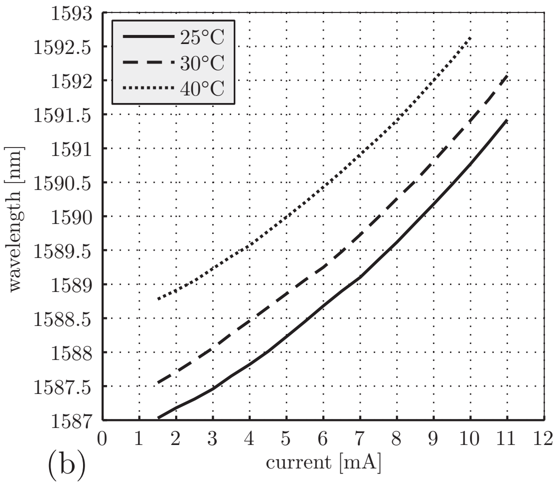

(b)

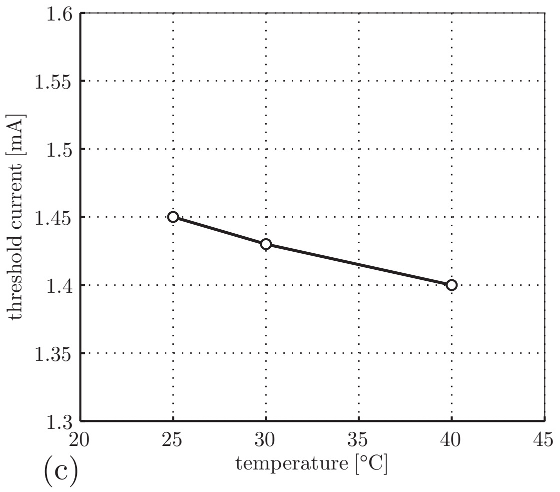

(c)

ambient temperature T_a [°C]	slope efficiency E_s [W/A]	differential resistance R_d [Ω]
25	0.122	53
30	0.117	53
40	0.104	52

(d)

Figure 2.8: Static characteristics at various temperatures of the 1591 nm VCSEL: (a) P-I and U-I characteristics, (b) wavelength vs. laser current, (c) threshold current vs. temperature, and (d) slope efficiency and differential resistance as a function of ambient temperature.

Unmodulated VCSEL wavelength spectra

In Fig. 2.9, I show the wavelength spectra of all four VCSELs at room temperature. The center wavelength is not exactly at the nominal channel wavelength, but the deviations, which are in the order of 3 nm, are acceptable because I used a broad channel spacing of 20 nm. Each of the single-mode lasers has a second emitting line, which is at least 33 dB lower than the main line and does not influence the system performance. Fig. 2.9(d) shows two spectra of the 1591 nm VCSEL. Usually, the line at lower wavelength is the main one, but this VCSEL changed its spectral line for bias currents above 3.8 mA.

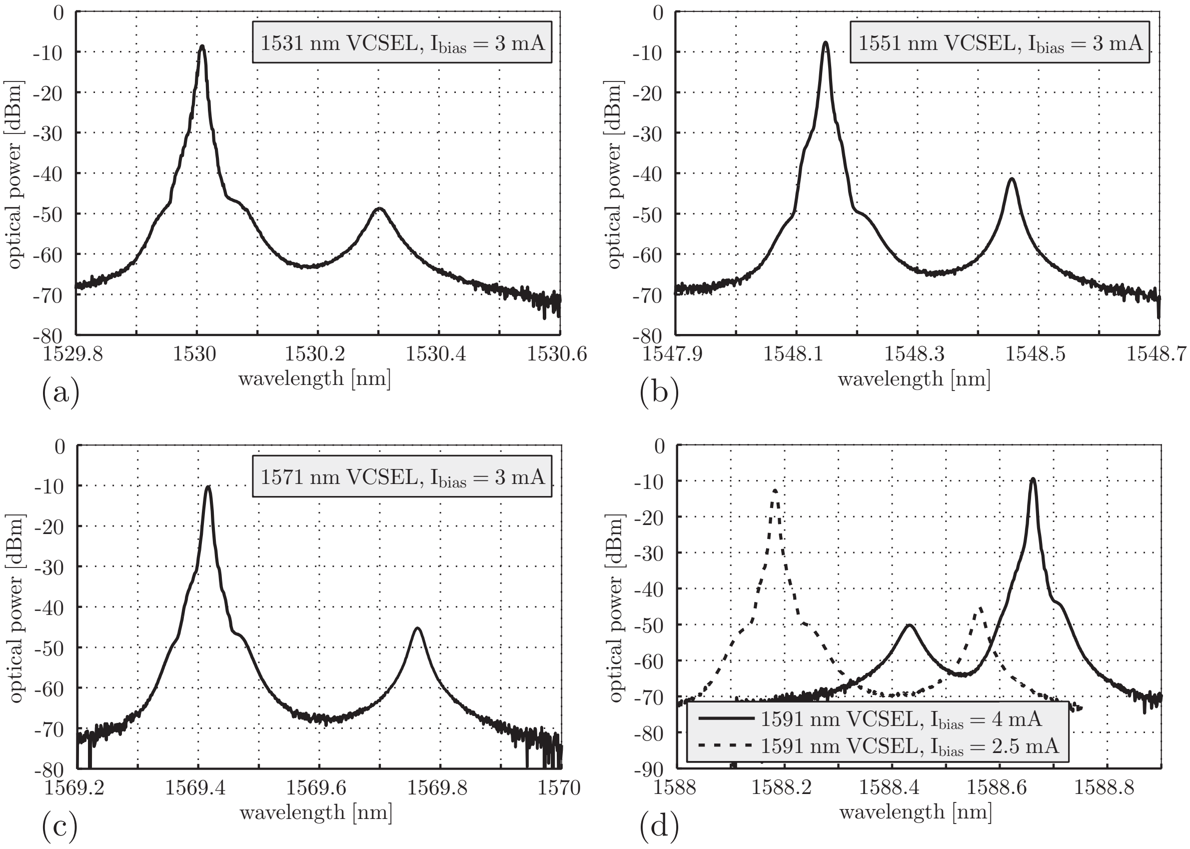

Figure 2.9: Unmodulated VCSEL spectra at room temperature $T = 23\,°\mathrm{C}$.

2.2.3 Dynamic characteristics of VCSELs

Figure 2.10 shows the measurement setup for the dynamic behavior of the four VCSELs used for the CWDM system.

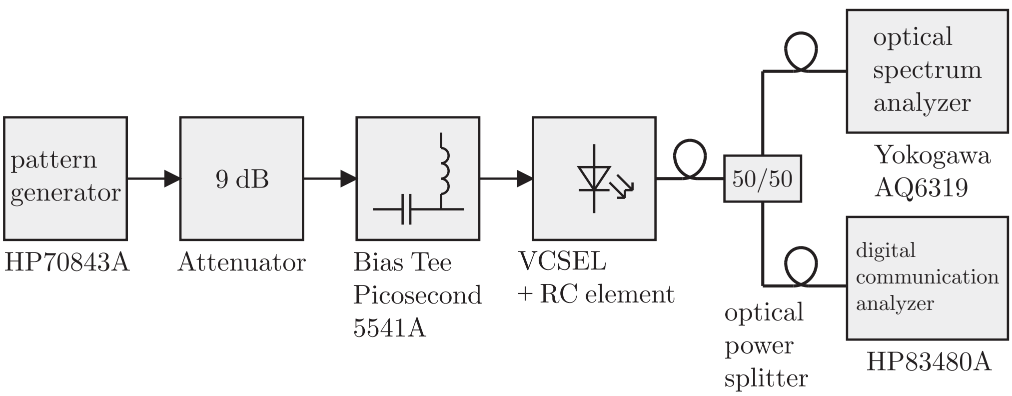

Figure 2.10: Measurement setup for dynamic characterization of the VCSELs.

The pigtailed TO-46 package of the VCSEL was mounted on a printed circuit board in series with a 50 Ω microstrip line, electrically connected with an SMA connector (cf. Fig. 2.11). Additionally, an RC element was placed close to the VCSEL (cf. Section 2.2.4). This element significantly improved the VCSEL's modulation response at frequencies above 3 GHz, which was originally limited mainly by the package. The anode contacts of the VCSELs were connected to the case, so the lasers were supplied with negative bias current to improve the radio frequency (RF) characteristics.

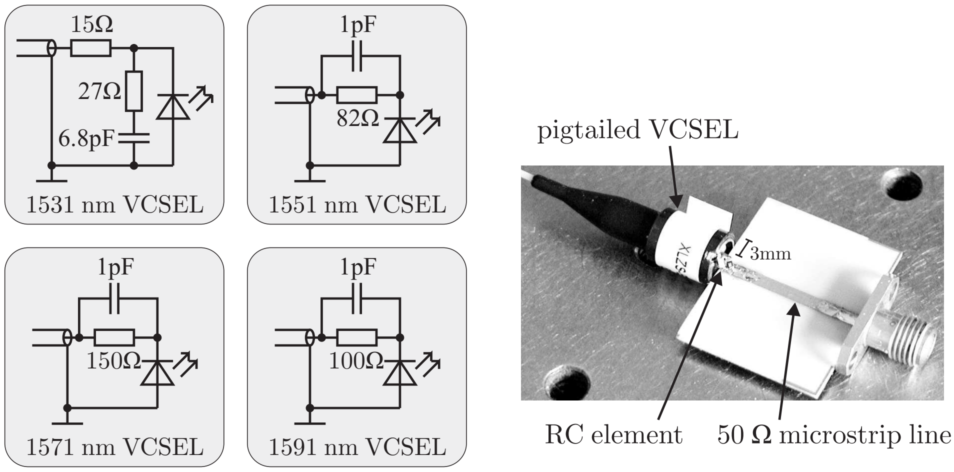

Figure 2.11: VCSEL mounting and RC elements.

Figure 2.12 shows the eye diagrams of the VCSELs for a data rate of 10.7 Gb/s with optimized RC elements at room temperature. The lasers are modulated with a *pseudo random bit sequence* (PRBS) pattern of length $2^{31} - 1$, the bias current I_{bias}, is 4 mA, except for the 1591 nm VCSEL ($I_{bias} = 5$ mA). The modulation swing at the pattern generator V_{PG}, is 1.2 V_{pp}, except for the 1531 nm VCSEL ($V_{PG} = 1.6\,V_{pp}$). The resulting extinction ratio of about 5.1 dB is rather small, due to a high bias current.

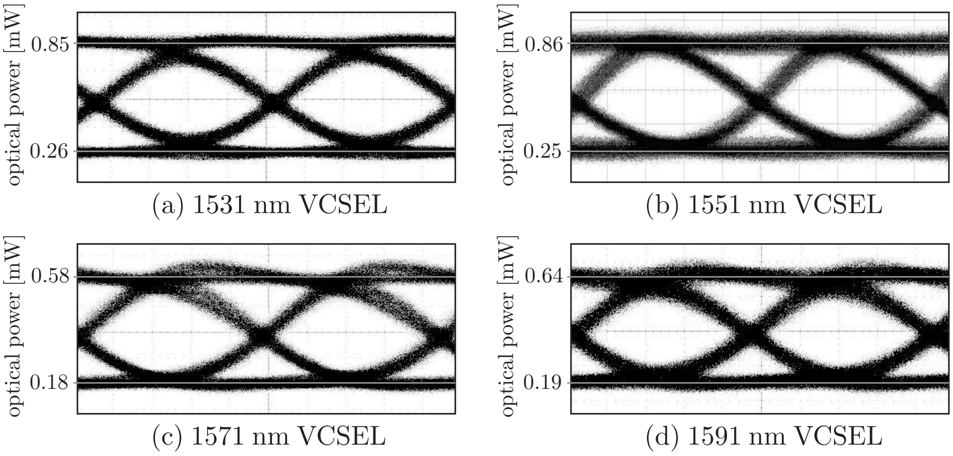

Figure 2.12: Eye diagrams of optimized VCSELs for 10.7 Gb/s at room temperature of 23 °C.

Wavelength spectrum and chirp of 1551 nm VCSEL

Figure 2.13 shows some optical wavelength spectra of the 1551 nm VCSEL for various driving conditions at room temperature $T = 22\,°\mathrm{C}$.

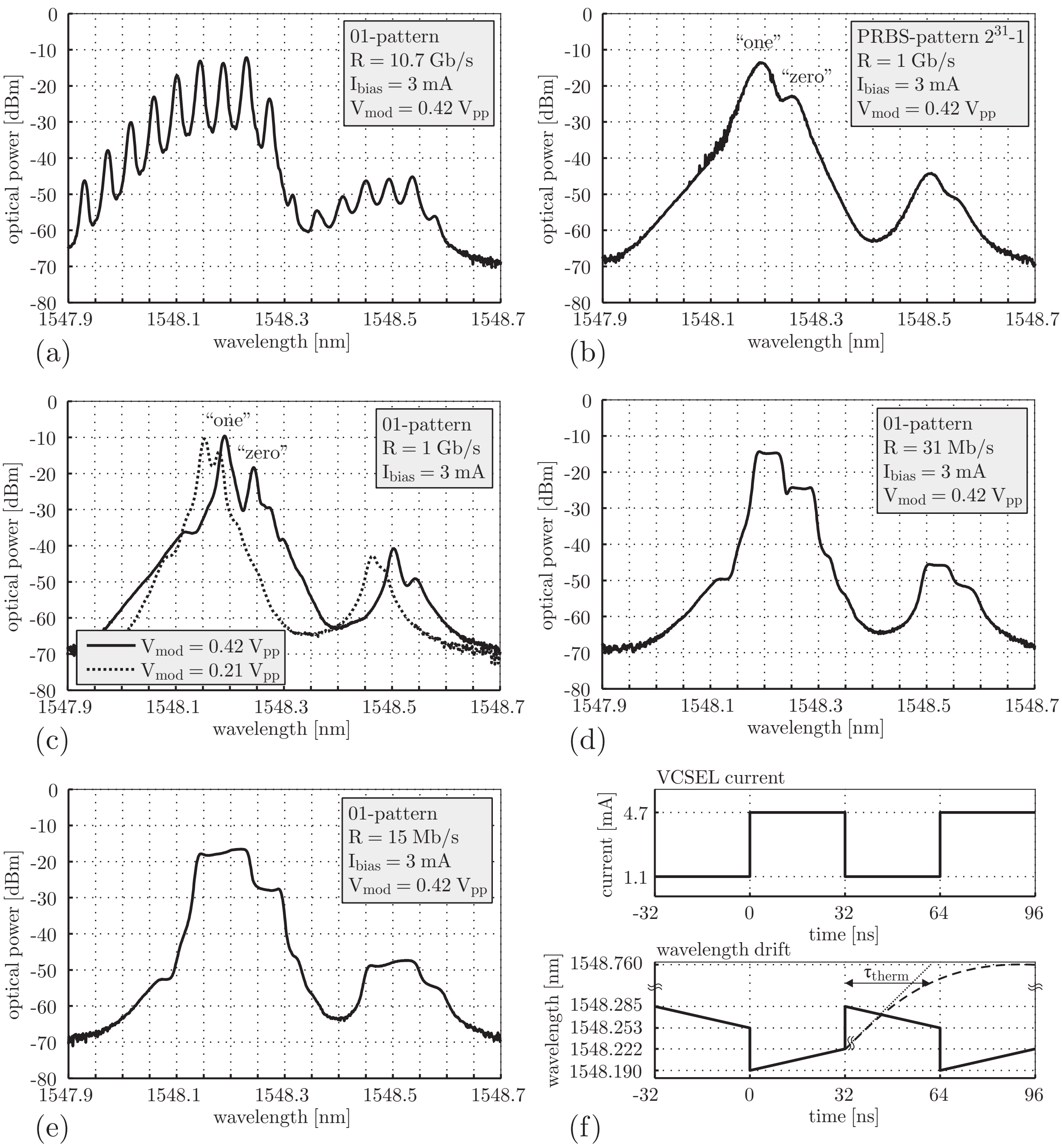

Figure 2.13: Modulated spectra and chirp of 1551 nm VCSEL at room temperature of $T = 22\,°\mathrm{C}$: (a) 10.7 Gb/s modulation using 01-pattern, (b) 1 Gb/s modulation using PRBS pattern of length $2^{31}-1$, (c) 1 Gb/s modulation using 01-pattern and different drive levels, (d) 31 Mb/s modulation using 01-pattern, (e) 15 Mb/s modulation using 01-pattern, (f) wavelength drift due to chirp and thermal impact at 31 Mb/s modulation using 01-pattern.

In Fig. 2.13(a), I depict the laser spectrum using modulation via a “0101” bit sequence pattern. The characteristic spectrum of a double side band amplitude modulation with a line spacing of $\frac{R}{2} = 5.35\,\text{GHz}$ (corresponding to 42.7 pm) can be seen. Part (b) shows the spectrum with a PRBS modulation at 1 Gb/s. The optical resolution of the optical spectrum analyzer of 10 pm is too large to see the modulation, but one can observe *adiabatic laser chirp*. Chirp is a frequency shift caused by changing refraction index and therefore different optical lengths of the active region in the VCSEL, due to varying currents for the “off” (“zero”) state and the “on” (“one”) state (cf. Fig. 2.13b). The propagation of chirped signals in dispersive fibers results in the conversion of optical *frequency modulation* (FM) into *intensity modulation* (IM). The impact on the CWDM system is shown in Section 3.1. Figure 2.13(c) depicts the situation for a 01-pattern and different driving voltages. The amount of chirp is depending on the modulation swing and the bias current. In Fig. 2.13(d) and (e) an additional thermal drift of the laser line for data rates below 50 Mb/s can be seen. The diagrams of Fig. 2.13(f) illustrate the time dependence of the wavelength for a low data rate of 31 Mb/s corresponding to part (d) of the figure. Beside the (chirp induced) rapid wavelength change of 63 pm, the thermal component of the wavelength drift here is $\frac{32\,\text{pm}}{32\,\text{ns}} = 1\,\text{pm/ns}$. In Fig. 2.13(f), the dashed line illustrates an exponential wavelength drift towards the wavelength value of the static thermal balance for an infinite “on” state of the VCSEL. This total wavelength drift is 0.57 nm, and thus, a very short thermal time constant for the small cavity of the VCSEL is determined.

$$\tau_{therm} = \frac{0.57\,\text{nm}}{1\,\text{pm/ns}} = 570\,\text{ns} \tag{2.1}$$

As a result, not only chirp and modulation broaden the optical signal spectrum, but also the thermal drift of the laser line for run lengths larger than 200 equal bits significantly increases the spectrum broadening. To avoid this, coding schemes with restricted maximum run lengths should be used.

Figure 2.14 depicts the influence of the adiabatic chirp of all four VCSELs at room temperature. The driving conditions were chosen for an extinction ratio of 9 dB. The lasers with longer wavelength had a smaller chirp compared to the ones with shorter wavelength.

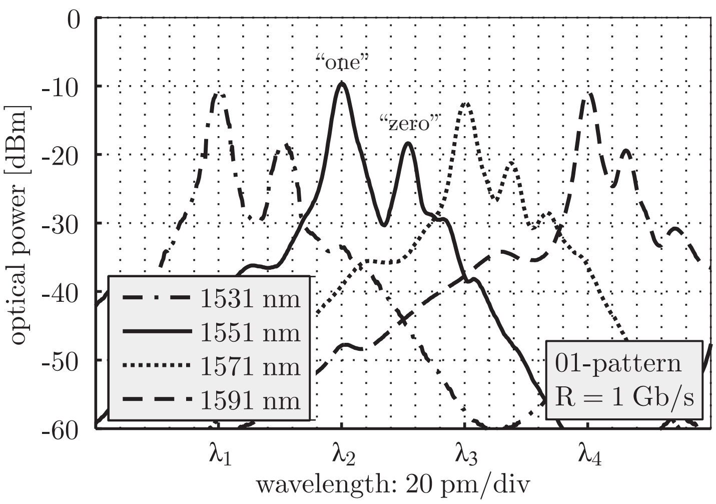

Figure 2.14: VCSEL chirp at room temperature $T = 22\,°\text{C}$ for extinction ratios of 9 dB.

Frequency response

The setup in Fig. 2.15 was used to measure the frequency response of the VCSELs including the RC element. A *vectorial network analyzer* (VNA) was used to directly modulate the laser with an electrical power level of $P_{RF} = -10\,\mathrm{dBm}$. This level was chosen low enough to avoid nonlinear behavior of the laser. The InGaAs pin-photodiode had a bandwidth of 55 GHz and a specified ripple in the frequency domain smaller than $\pm 0.3\,\mathrm{dB}$. The electrical frequency response, measured with the VNA, was transformed to an optical one[1].

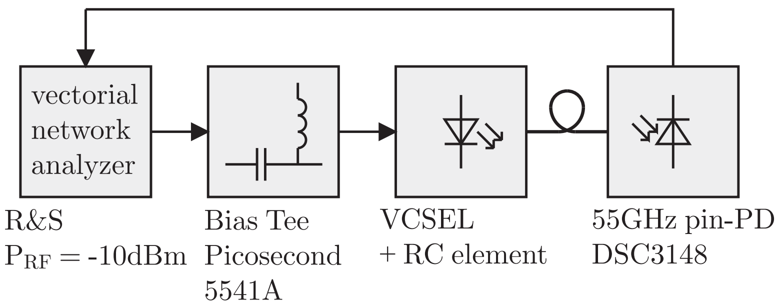

Figure 2.15: Setup for frequency response measurement.

Figure 2.16 and Fig. 2.17 show the optical frequency response and the electrical return loss of the VCSELs including RC element and microstrip line. The curves were normalized to the values at a frequency of 0.2 GHz.
High bias current (Fig. 2.16) lead to significantly higher 3 dB-bandwidths compared to low bias current (Fig. 2.17). The electrical reflection is rather high, but an optimal return loss was not the main goal of the RC element added to the VCSEL. The reflected electrical power was terminated in the matched source resistance, so it had no influence to the CWDM system performance. Instead, the RC element was designed for a flat frequency response to increase the modulation performance for high frequencies. The VCSEL's 3 dB-bandwidth without RC element was some 4 GHz due to package limitations.

[1]The photodiode converts optical power into electrical current. Thus, the relative electrical power levels measured, are squares of the corresponding optical power levels.

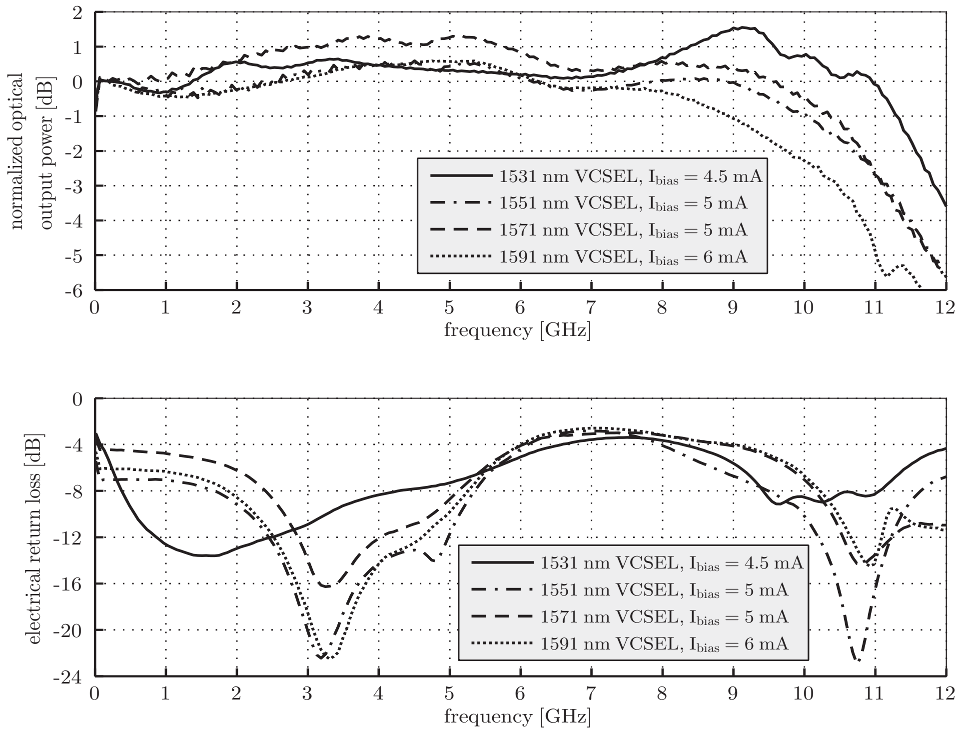

Figure 2.16: Frequency responses and electrical return losses for all four VCSELs at high bias.

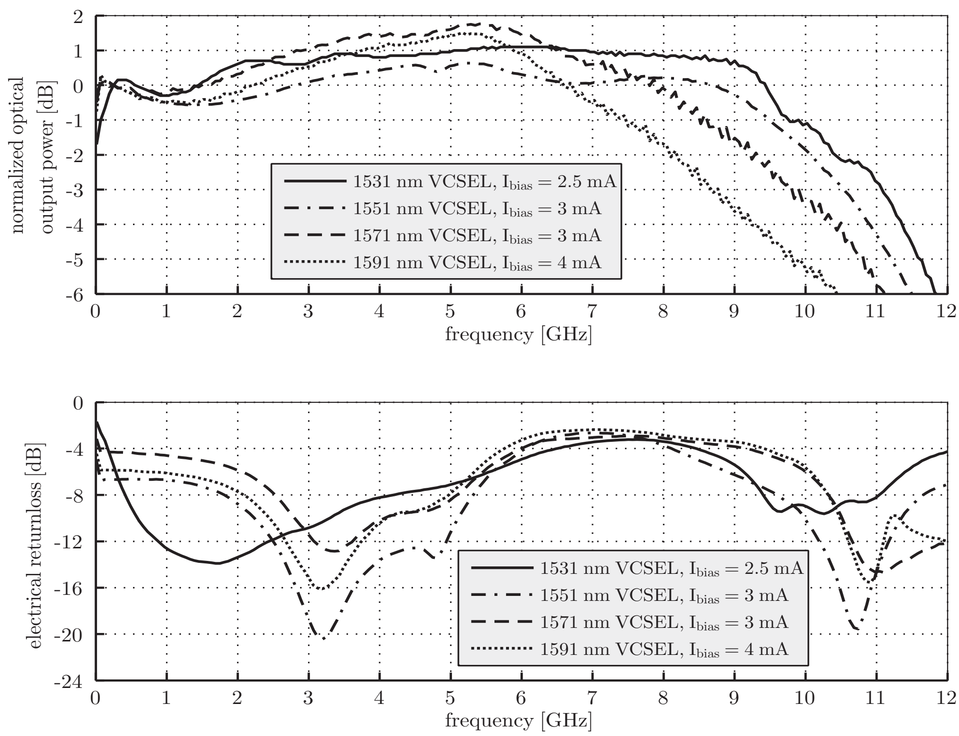

Figure 2.17: Frequency responses and electrical return losses for all four VCSELs at low bias.

Table 2.2 summarizes the main dynamic characteristics of the four VCSELs at room temperature $T = 23\,°\mathrm{C}$ for a data rate of 10.7 Gb/s.

VCSEL	rise time t_r [ps]	fall time t_f [ps]	bandwith B [GHz]	achievable extinction ratio E_x [dB]
1531 nm	39	52	11.4	8.6
1551 nm	32	50	10.9	9.9
1571 nm	44	48	10.7	9.0
1591 nm	40	48	10.2	9.1

Table 2.2: VCSEL's dynamic characteristics at 10.7 Gb/s.

2.2.4 VCSEL's modulation response optimization

As described in Section 2.2.3, an RC element was added to the VCSEL to improve its modulation response at high frequencies. In this section, I present the process of dimensioning this element and optimizing the frequency response when using a 1591 nm VCSEL. Figure 2.18 depicts an experiment, where the VCSEL was mounted at the end of a 50 Ω microstrip line.

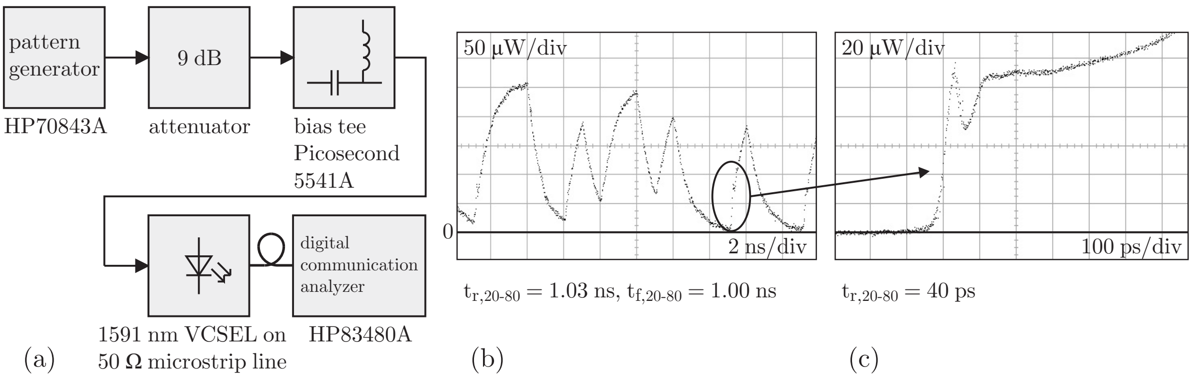

Figure 2.18: (a) Setup for rise and fall time measurements. (b) Optical output power vs. time at low bias current. (c) Detail of diagram (b) at a low bias current.

Modulating the VCSEL with a PRBS pattern lead to rise and fall times in the range of 1 ns (cf. Fig. 2.18b). Therefore, the dynamic behavior of the laser without any modifications was unsuitable for modulation at 10 Gb/s. Part (c) of Fig. 2.18 shows a detail of the diagram (b), but at a 20 times faster scale. The bias current here was very low, so that sometimes the current fell below the threshold current. From this point, the VCSEL turned on rapidly with a rise time of 40 ps and a fast optical relaxation oscillation was visible. I concluded that the optical part of the laser was fast enough for 10 Gb/s operation, but the electrical bandwidth seemed to be limited by an intrinsic parasitic capacity, that produced the exponential curves shown in Fig. 2.18(b).

As one can see in Fig. 2.19(a), the VCSEL was mounted into a TO-46 package and its anode was contacted to the ground of the case. To avoid additional capacitance and bandwidth loss, the VCSEL was biased negatively, so the RF-contact corresponded to the cathode.

Figure 2.19(b) shows the equivalent RF-schematic of the laser including the main electrical parasitic elements. The inductance L_{wire} of approximately 1 nH was caused by a 1 mm wire from the case to the microstrip line. Beside the small capacitance of the case $C_{case} \approx 0.5\,\text{pF}$, the differential resistance $R_d = 75\,\Omega$ of the VCSEL, and the relative large inductance $L_{bond} \approx 2\,\text{nH}$ of the 2 mm bonding wire, the huge intrinsic capacitance of $C_{VCSEL} \approx 10\,\text{pF}$ was the main reason for bandwidth limitation.

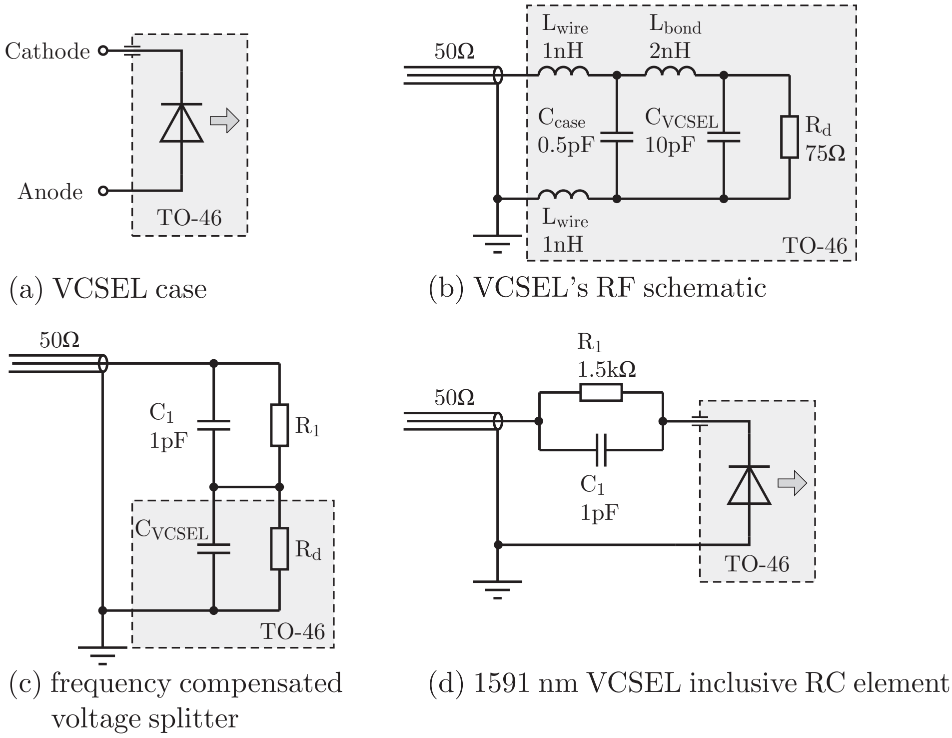

(a) VCSEL case

(b) VCSEL's RF schematic

(c) frequency compensated voltage splitter

(d) 1591 nm VCSEL inclusive RC element

Figure 2.19: (a) TO-46 case of VCSEL, (b) RF-schematic of 1591 nm VCSEL including parasitic elements, (c) principle of frequency compensated voltage splitter, (d) optimal RC element for the 1591 nm VCSEL.

To compensate the influence of C_{VCSEL}, the principle of a frequency compensated voltage splitter (Fig. 2.19c) was used. The time constant of $\tau_1 = R_1 \cdot C_1$ had to be equal to the time constant of $\tau_{VCSEL} = R_d \cdot C_{VCSEL}$. A second requirement for short rise and fall times of at most 50 ps for non problematic 10 Gb/s operation, is a small capacitance C_1. This is because of the resulting RC low pass filter consisting of the $50\,\Omega$ source resistance from the microstrip line and the input capacitance of the whole schematic. This means, that the time constant $\tau_{source} = R_{source} \cdot C_1$ must be in the range of 50 ps, leading to

$$C_1 = \frac{\tau_{source}}{R_{source}} = \frac{50\,\text{ps}}{50\,\Omega} = 1\,\text{pF} \quad \text{and} \tag{2.2}$$

$$R_1 = \frac{R_d \cdot C_{VCSEL}}{C_1} = \frac{75\,\Omega \cdot 10\,\text{pF}}{1\,\text{pF}} = 750\,\Omega. \tag{2.3}$$

Figure 2.19(d) shows the final circuit for this 1591 nm VCSEL. The value of R_1 was optimized for overall frequency response and thus changed to $1.5\,\text{k}\Omega$, because of the additional influence of other parasitic elements.

In Fig. 2.20(a), the measurement of a frequency spectrum via a *fast fourier transformation* (FFT) is demonstrated. The graph depicts the spectrum of a PRBS pattern with length 2^7-1 at 10 Gb/s, generated by a 4096 point FFT with flat-top windowing. A detailed *discrete fourier transformation* (DFT) analysis of the PRBS generator polynomial x^7+x^6+1 resulted in an exactly white sequence and thus the short PRBS of length 2^7-1 could be used for frequency measurements via FFT. This method for determining the frequency characteristics was used instead of a network analyzer, because it was an efficient possibility to switch from the time domain to the frequency domain and vice versa in short time. Part (b) of Fig. 2.20 depicts the FFT generated optical frequency response of the 1591 nm VCSEL leading to a 3 dB-bandwidth of approximately 4 GHz.

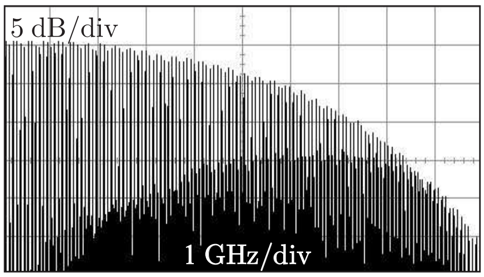

(a) 4096 point FFT of 10 Gb/s PRBS pattern of length 2^7-1

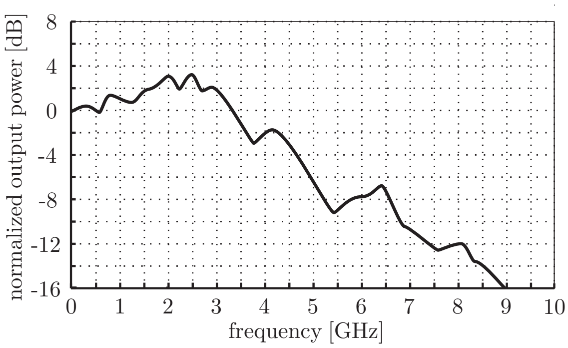

(b) power spectrum of modulated 1591 nm VCSEL

Figure 2.20: (a) FFT frequency response of not bandlimited PRBS pattern, (b) optical frequency response of modulated VCSEL including RC element.

The power spectrum of Fig. 2.20(b) should ideally look like the spectrum of the PRBS pattern in part (a) of the figure, but various electrical resonances especially at 2.5 GHz lead to signal degradation also in the time domain. Nevertheless, the modulation performance of the VCSEL including the RC element increased, and the switching times reduced by a factor of 9 compared to the VCSEL without RC element (cf. Fig. 2.23). Practical experience showed good performance of the VCSEL's modulation response, if the optical frequency response is close to the ideal one of Fig. 2.20(a). Therefore, an electrical filter was designed to pre-distort the signal and to compensate the resonance in the VCSEL's frequency response.

Figure 2.21 shows the setup for optimum modulation response of the 1591 nm VCSEL. The used filter (cf. Fig. 2.22a) and the amplifier were followed by an attenuator for impedance matching.

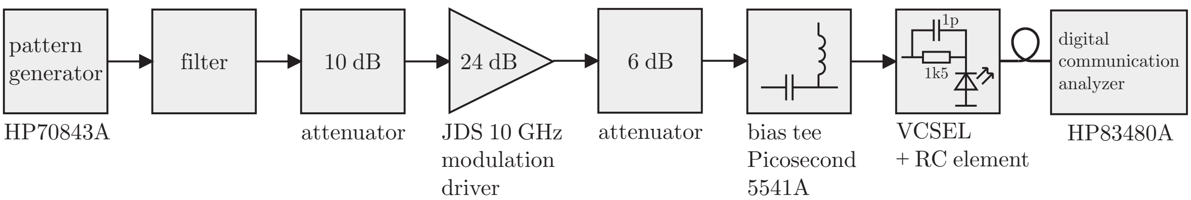

Figure 2.21: Setup for optimal modulation response for the 1591 nm VCSEL.

In Fig. 2.22, the schematic as well as the frequency response of the used filter are depicted. The main part of the filter was a series resonator consisting of L_2, C_2, and R_2. It compensated the peak in the response of the VCSEL at 2.5 GHz. R_3 and C_3 formed a high pass filter to attenuate frequencies below 4 GHz for a flat overall frequency response. R_1 and C_1 finally compensated the high pass characteristic of the amplifier. The filter was implemented with small "0603" (1.5×0.75 mm) components to avoid wave propagation between them. As the image in Fig. 2.22(b) shows, the inductance L_2 was realized as piece of wire of approximately 5 mm length.

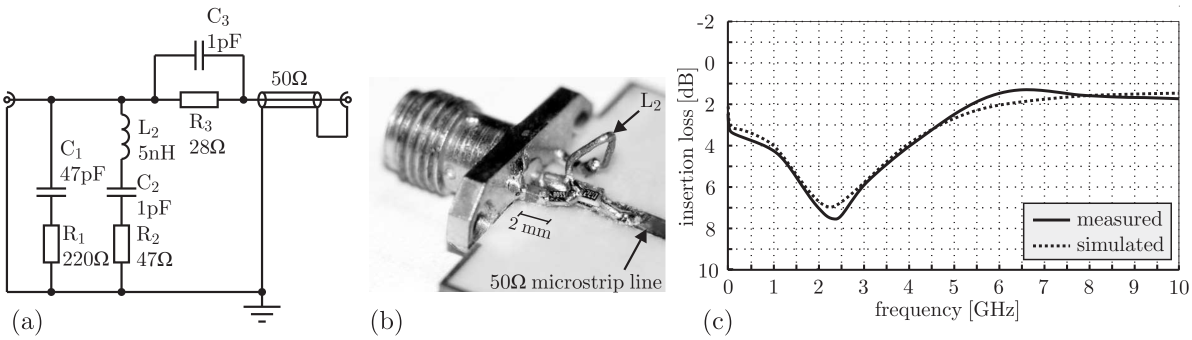

Figure 2.22: (a) Schematic, (b) image, and (c) measured and simulated frequency response of the filter.

Figure 2.23 summarizes the bandwidth optimization of the 1591 nm VCSEL and presents its eye diagrams for different data rates from 1 Gb/s to 10.7 Gb/s.

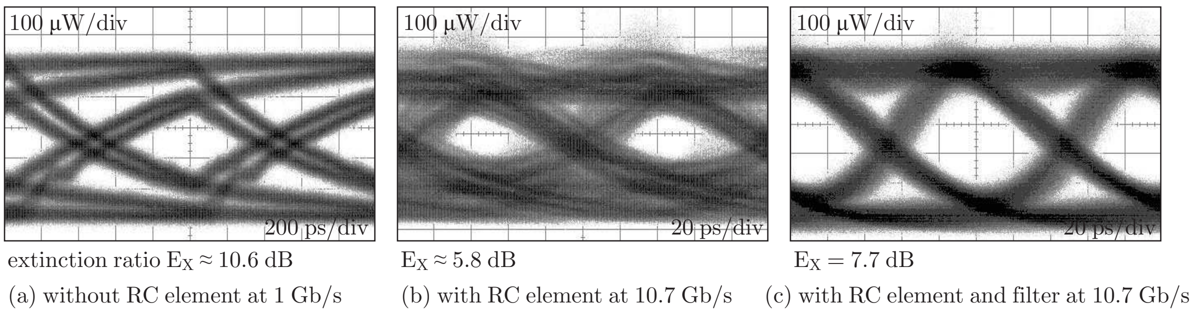

Figure 2.23: Eye diagrams of the 1591 nm VCSEL: (a) without RC element, (b) inclusive RC element, (c) including RC element and filter.

The intrinsic capacitance C_{VCSEL} of the VCSELs, which were used for the CWDM system, was much smaller, so the use of an RC element was sufficient. No additional filter and no time intensive optimization were necessary. The RC element compensated the bandwidth limitation due to L_{wire}, C_{case}, and L_{bond}, which was mainly caused by the TO-46 package. The exact values of the RC elements are shown in Fig. 2.11.

Figure 2.24 presents the eye diagrams of all four VCSELs without RC elements in the first row. The final eye diagrams including RC elements are shown in the second row.

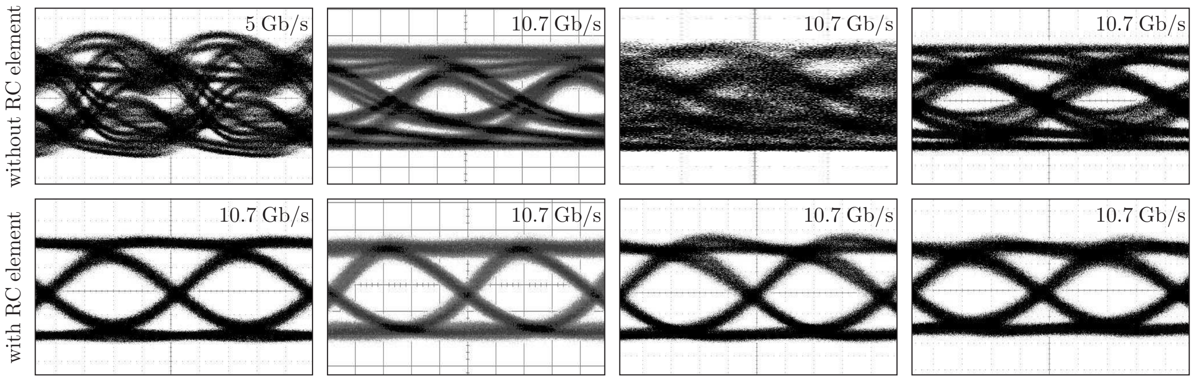

(a) 1531 nm VCSEL (b) 1551 nm VCSEL (c) 1571 nm VCSEL (d) 1591 nm VCSEL

Figure 2.24: Eye diagrams of VCSELs without RC elements (first row), and including RC elements (second row).

2.3 Standard single-mode fiber (SSMF)

Fiber loss is – beside dispersion – the main limiting factor for optical transmission systems. The attenuation coefficient of the fiber α_T [dB/km] depends on the wavelength and the dominating losses are material absorption and Rayleigh scattering. Material absorption in SSMF is mainly caused by the presence of water vapors. A resonance of the OH^- ions produces an absorption peak around 1380 nm, which is commonly called *water peak* [12].

Figure 2.25 shows the characteristics of the SSMF used in the CWDM system. I used such a fiber to transmit the CWDM signals over the low-loss wavelength range from 1531 nm to 1591 nm. These upper channels have the disadvantage of rather high dispersion of about 17 ps/nm.km, which causes broadening of the pulses.

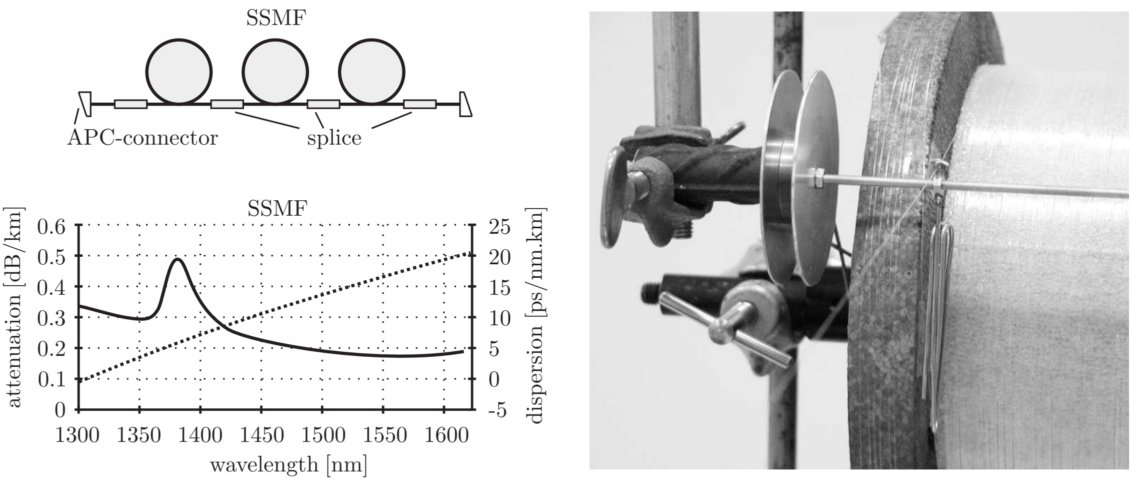

Figure 2.25: SSMF characteristics [13].

I prepared some spools of fiber with different length to be able to do measurements for several fiber distances. The photo in Fig. 2.25 shows a fiber spool with 5 km of fiber which was winded manually. The apparatus was necessary to avoid additional bending loss of the fiber due to micro bending caused by the layered stack. Single-mode pigtailed angled physical contact (FC/APC) connectors were spliced onto the ends of the fiber spools.

As you can see in Table 2.3, the used SSMF had a slightly higher absorption coefficient than the one depicted in Fig. 2.25 from *Corning* [13].

		attenuation					
spool number	length	complete	coefficient (incl. splice)	APC-con. 1 (incl. splice)	splice 1 splice 1	splice 2 splice 2	APC-con. 2 (incl. splice)
No.1 (white)	77.2 km	17.69 dB	0.225 dB/km	0.11 dB	0.48 dB	0.11 dB	0.10 dB
No.2 (white)	51.4 km	11.46 dB	0.213 dB/km	0.17 dB	0.11 dB		0.33 dB
No.3 (white)	25.65 km	5.87 dB	0.211 dB/km	0.23 dB			0.27 dB
No.4 (blue large)	14.18 km	3.29 dB	0.211 dB/km	0.14 dB			0.21 dB
No.5 (red large)	10.79 km	2.52 dB	0.200 dB/km	0.14 dB			0.23 dB
No.6 (blue small)	5.04 km	1.36 dB	0.209 dB/km	0.11 dB			0.20 dB
No.7 (red small)	2.16 km	1.25 dB	0.284 dB/km	0.31 dB	0.12 dB		0.47 dB
No.8 (blue small)	1.14 km	0.82 dB	0.218 dB/km	0.34 dB			0.29 dB

Table 2.3: Measured characteristics of the used SSMFs at 1550 nm.

2.4 Multiplexer

An amplifier-free configuration of CWDM systems requires low insertion losses of the used components. On the other hand, the wide possible wavelength variation of the transmitting laser requires a wide and flat channel passband. Moreover, the multiplexing/demultiplexing filter should be compact and inexpensive.

This can be done by using *thin film* technology, which is well known and easy to process, leading to low costs. *Thin film filters* (TFFs) have a good spectral response combined with low insertion loss. The technology uses thin layers of dielectric material of different refraction index to build wavelength dependent wave guides with passband character [14].
The 8-channel *multiplexing* (MUX) and *demuliplexing* (DEMUX) filters[2] used in the CWDM system are manufactured by *Browave Corporation* [15].

Figure 2.26(a) and (c) show the measurement setup and the insertion loss of the 1551 nm channel of the multiplexer. This measurement was done via a tuneable laser source combined with the "max.-hold" function of the *optical spectrum analyzer* (OSA). So a high dynamic range was achieved to measure the isolation characteristic in the adjoining channels. Figure 2.27 depicts the transmission characteristics of the multiplexing and demultiplexing filters, which were measured with a white light source. Table 2.4 lists the insertion losses for the multiplexer and the demultiplexer at the VCSEL's emission wavelengths.

[2] A data sheet of the used MUX/DEMUX filters can be found in appendix A.

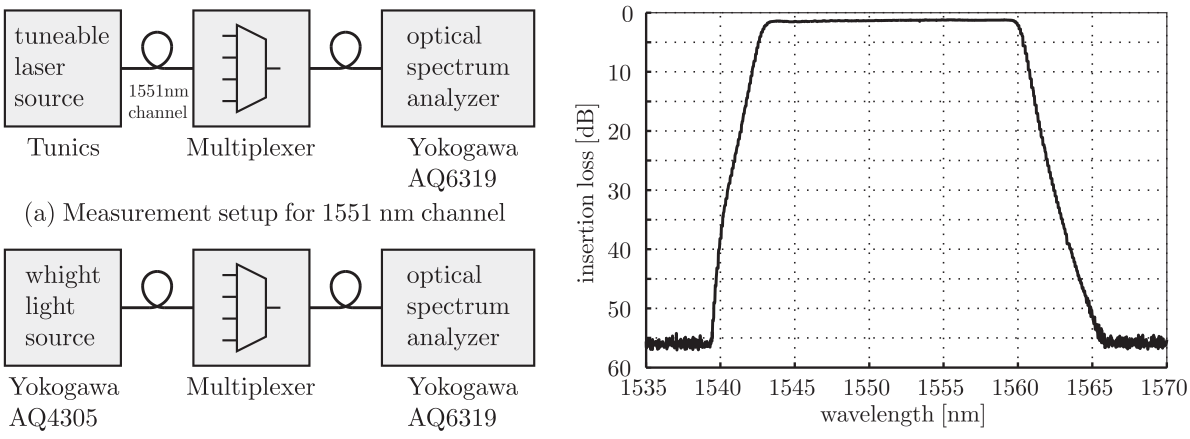

(a) Measurement setup for 1551 nm channel

(b) Measurement setup for all channels

(c) Multiplexer insertion loss for 1551 nm channel

Figure 2.26: (a, b) Measurement setups, and (c) isolation characteristic for the 1551 nm channel.

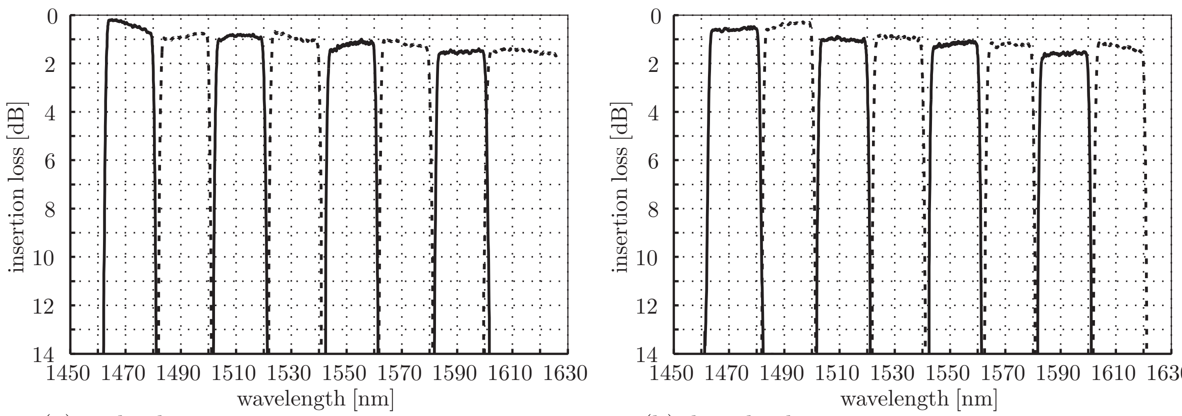

(a) multiplexer

(b) demultiplexer

Figure 2.27: Filter characteristics of CWDM thin film multiplexers at room temperature $T = 25\,°C$.

VCSEL	emission wavelength	multiplexer	demultiplexer
1531 nm	1530.1 nm	0.97 dB	0.85 dB
1551 nm	1548.7 nm	1.36 dB	1.08 dB
1571 nm	1569.8 nm	1.41 dB	1.28 dB
1591 nm	1589.2 nm	1.47 dB	1.78 dB

Table 2.4: Insertion losses of CWDM thin film multiplexers at VCSEL's emission wavelength at room temperature $T = 25\,°C$.

2.5 Receiver

The two main types of photodiodes used for direct detection receivers are the pin-diode and the *avalanche photodiode* (APD). While InGaAs pin-diodes – used for 1.55 μm wavelength – are cheap, APDs have a higher sensitivity due to photoelectron multiplication in the avalanche region. Therefore, loss limited systems profit from the use of APD-receivers.

2.5.1 Pin-receiver

In the CWDM system I used a pigtailed pin-receiver[3] from Ortel (now Lucent). This DC-coupled receiver contained a pin-photodiode with a sensitivity of 0.8 A/W, a *transimpedance amplifier* (TIA) and a limiting amplifier, optimized for a data rate of 10 Gb/s.

Figure 2.28 shows the setup for a back-to-back receiver sensitivity measurement at room temperature. Figure 2.29 presents the corresponding results for all four VCSELs at a data rate of 10.7 Gb/s. The datasheet of the receiver specifies a sensitivity of -18 dBm at a BER of 10^{-10}, but the sensitivity measurement with the VCSELs did not reach this value. To find out the reason for the difference, the sensitivities for various driving conditions of the 1591 nm VCSEL were determined. The solid line with circular marks in Fig. 2.30 represents the sensitivity curve measured with PRBS pattern modulation at 10.7 Gb/s. The curve with rectangular marks shows a similar situation, but using a pattern consisting of a "0101" bit sequence. This deterministic modulation eliminated the possible *inter symbol interference* (ISI) caused by the bandlimited VCSEL, and only the influence of the receiver amplifier induced electrical noise remained. So the measured curve decreased faster, compared to the one for the PRBS pattern, and its shape was similar to the Q-function (thin dotted line). The driving conditions for the VCSEL for both measurements were optimized for maximum sensitivity, and this resulted in a reduced bias current for the measurement with the 01-pattern. The resulting noise-limited receiver sensitivity curve reached the specified value in the datasheet. The dashed lines in Fig. 2.30 show an equivalent situation for a data rate of 2.5 Gb/s.

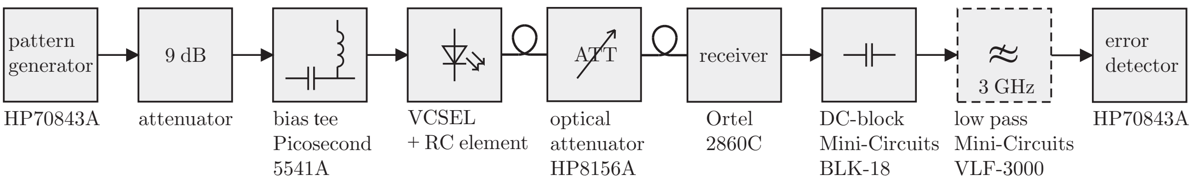

Figure 2.28: Setup for receiver sensitivity measurement

[3] A data sheet of the Ortel 2860C can be found in appendix A.

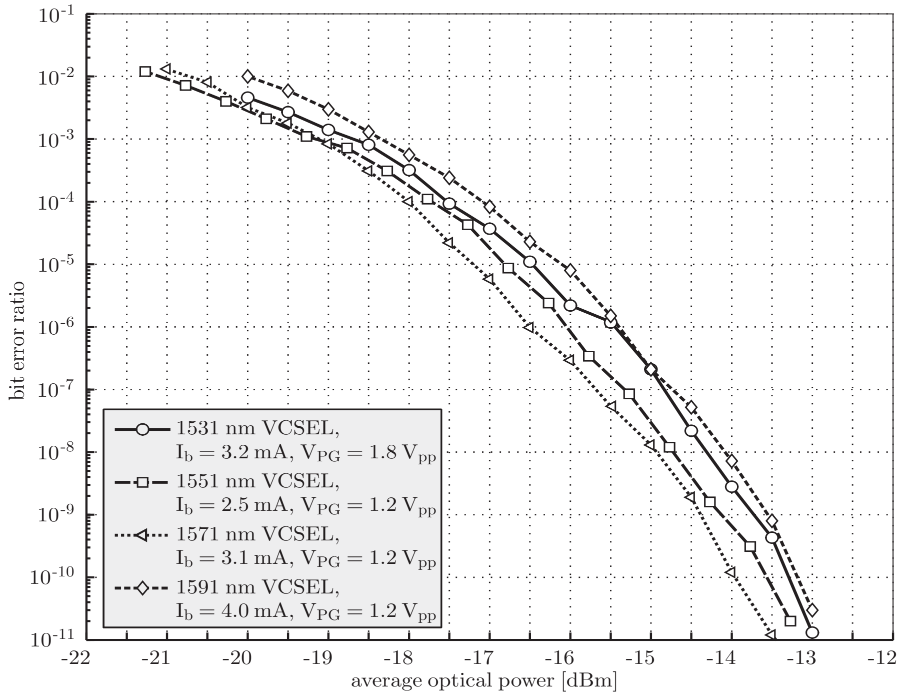

Figure 2.29: Back-to-back receiver sensitivities measured with all four VCSELs at 10.7 Gb/s with a PRBS pattern of length $2^{31} - 1$.

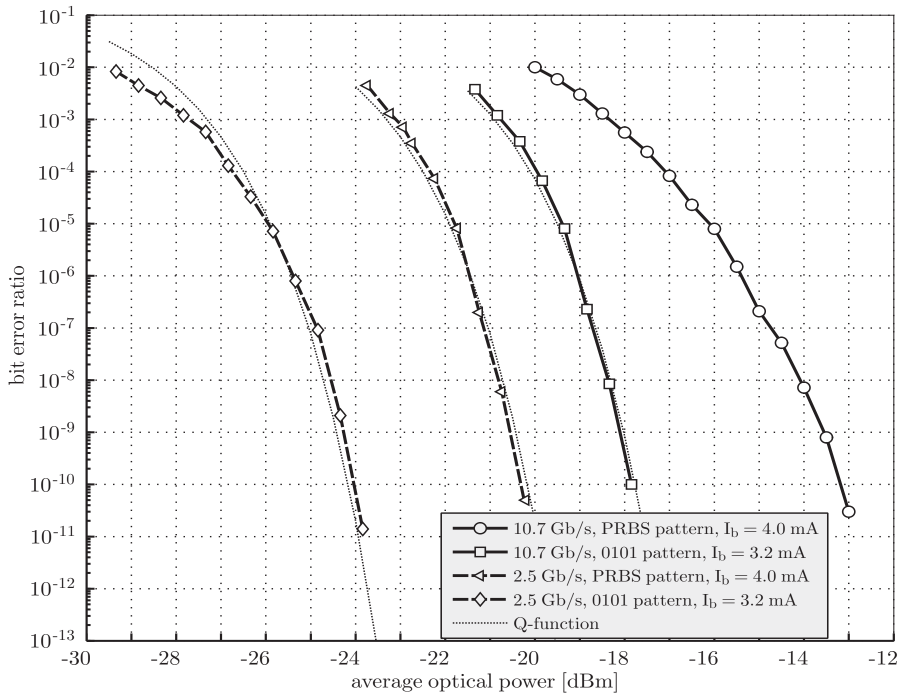

Figure 2.30: Back-to-back receiver sensitivities measured with the 1591 nm VCSEL using a 0101-pattern and a PRBS pattern with the length $2^{31} - 1$.

To verify that the performance of the system is not severely degraded by the receiver, its frequency response was measured. Figure 2.31 shows the setup and the frequency response of the pin-receiver. The measurement was done via a comparison of the *fast fourier transformation* (FFT) of both the optical and the electrical signal captured by the digital communication analyzer (DCA). The solid line, depicted in the diagram, results from FFT magnitude analysis of the first order wave when using a “0101” bit sequence pattern. To check for nonlinearities, the modulation voltage V_{PG} was doubled for the dashed curve in Fig. 2.31(b), and the dotted line resulted from an FFT magnitude measurement of the whole spectrum when using a PRBS pattern of length $2^7 - 1$. In consideration of the VCSEL’s frequency responses, the behavior of the receiver is acceptable.

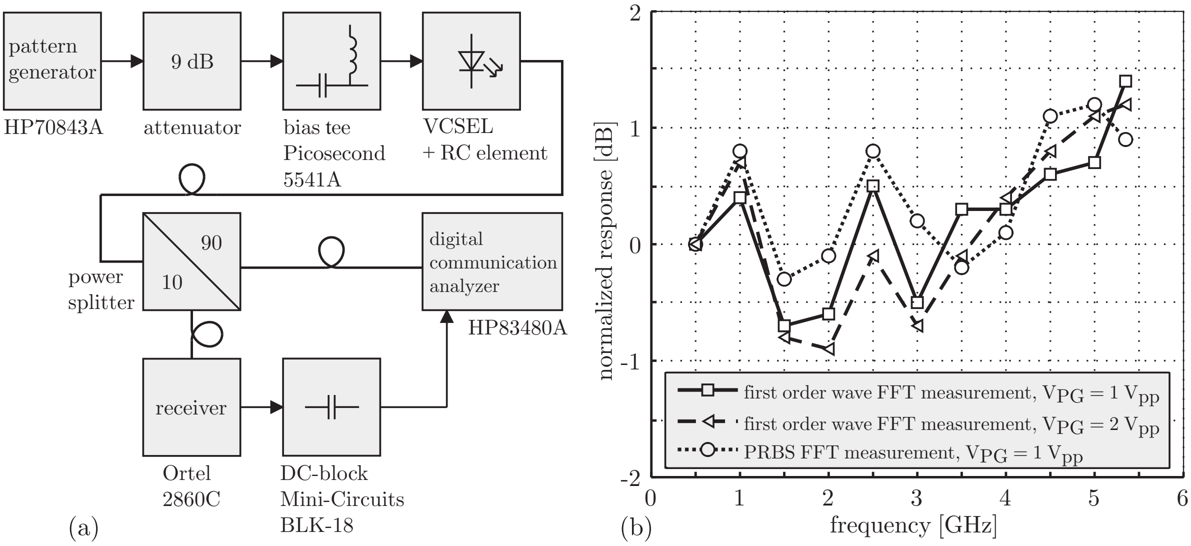

Figure 2.31: (a) Setup for measuring the frequency response (b) of the receiver.

2.5.2 Comparison with APD-receiver

APD-receivers have a higher sensitivity when compared to conventional pin-receivers due to photoelectron multiplication. Table 2.5 lists some manufacturers of APD- and pin-receivers and compares their sensitivities.

manufacturer	APD-RX sens. ($BER = 10^{-12}$)	pin-RX sens. ($BER = 10^{-12}$)
Hamamatsu	-27.7 dBm	-20 dBm
Northlight Optronics	-27 dBm	-20 dBm
CyOptics	-27 dBm	-19 dBm

Table 2.5: Examples of APD-/pin-receivers and their sensitivities at 10 Gb/s [16, 17, 18].

2.6 Characteristics of electrical components

To verify the characteristics of the electrical components used in the system, their frequency responses were measured. Figure 2.32(a) depicts the characteristics of various bias tees from

Picosecond Pulse Labs and *Mini Circuits*. Model 5541A was used for the main channel in the CWDM system, because of its flat response. Various tests including bias tee model 5542 resulted in significant performance degradation, so it was not used for further experiments. Part (b) of Fig. 2.32 shows the response of the DC-block used after the DC-coupled receiver. Its lower cut off frequency of 1.5 MHz was sufficient for high data rate measurements. The relative high frequency dependent attenuation of 50 cm high quality coaxial cable (RG223) acted as low pass filter, so the cable length was kept as short as possible. Figure 2.32(c) and (d) depict the frequency response of the power splitter and the 3 GHz low pass filter used for 2.5 Gb/s measurements.

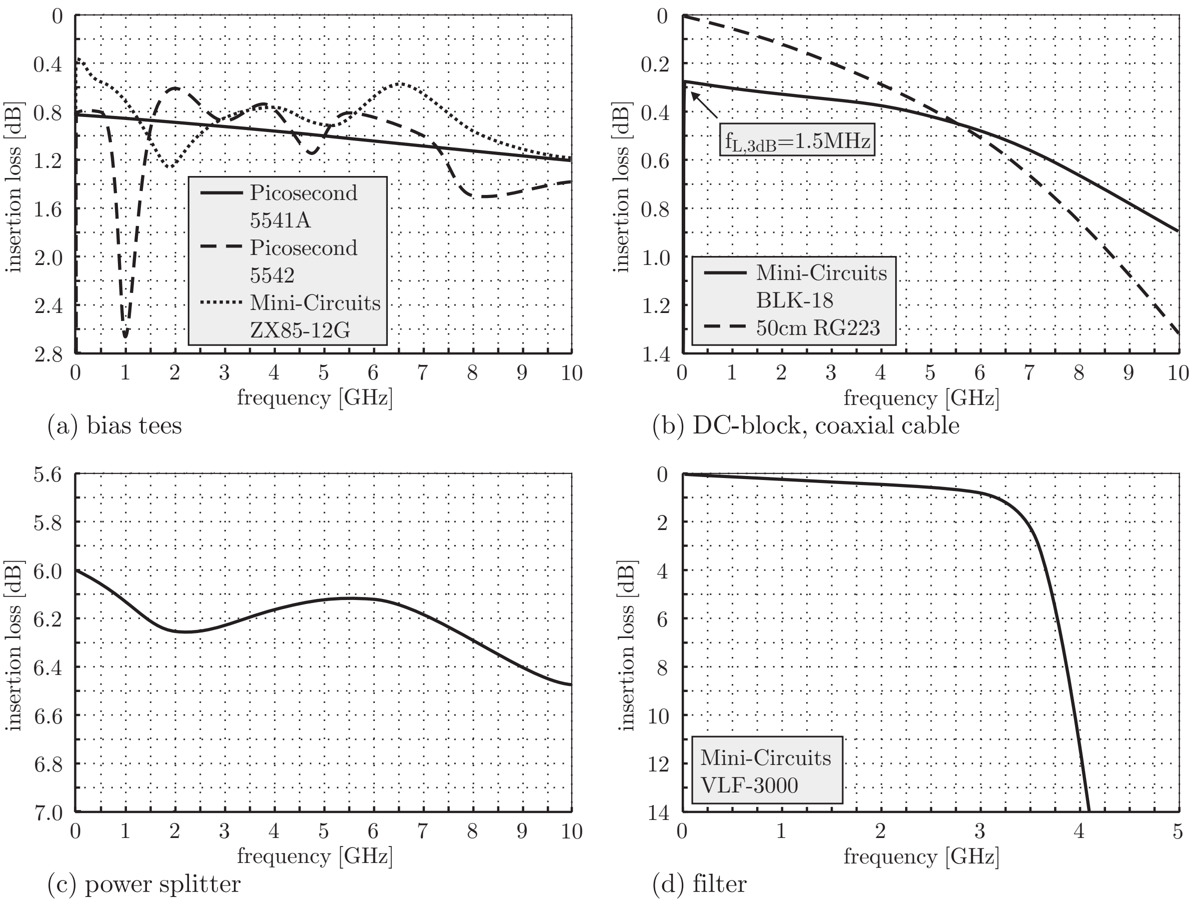

Figure 2.32: Frequency response of (a) bias tees, (b) DC-block BLK-18 and 50 cm coaxial cable, (c) power splitter and (d) low pass filter VLF3000.

2.7 Conclusion

Directly modulated long wavelength VCSELs, thin film filters, standard single mode fibers, and pin-receivers, necessary for my CWDM experiments are all commercial available and have a good price-performance ratio. To enhance the performance in such systems, forward error correction can be used. Today's FEC hardware is rather expensive, but advances in semiconductor and integrated circuit (IC) technology will decrease the costs.

Chapter 3

CWDM experiments

In the previous chapter, I described the main characteristics of the components used for the CWDM system. Effects leading to signal degradation like loss, dispersion and chirp were explained, and the possibility of forward error correction for performance enhancement was outlined.

In this chapter, I present the performance of the overall system for a single channel as well as for multiple channel operation.

3.1 Single channel transmission system

This section contains the results of a single channel transmission system at 1551 nm wavelength and a data rate of 10.7 Gb/s, using SSMF.

3.1.1 System setup and results

Figure 3.1 shows the setup for the single channel system. The transmission media consisted of some spools of SSMF, which were connected together via APC connectors to realize variable lengths of fiber. Thus, the overall fiber attenuation increased due to the accumulated connection losses. An *Erbium doped fiber amplifier* (EDFA) was added to the setup in order to emulate a VCSEL with increased output power for future generations of devices.

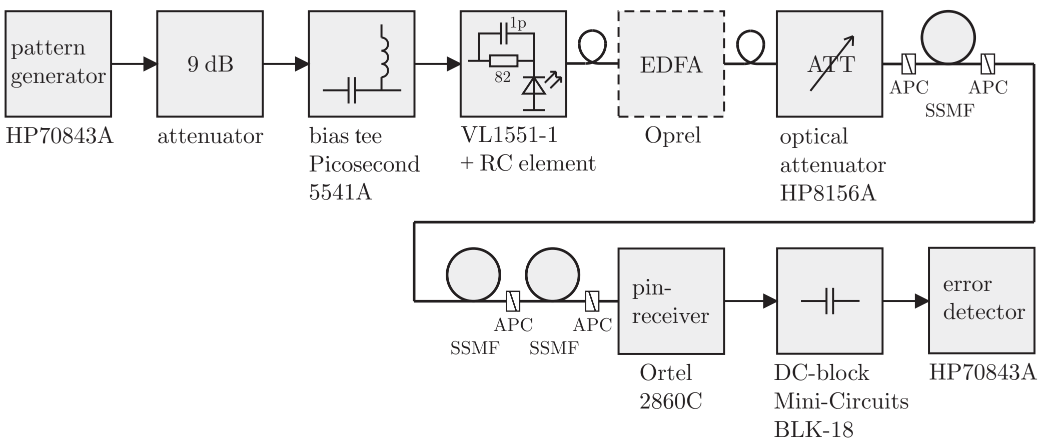

Figure 3.1: Single channel system setup.

Figure 3.2 depicts, as a typical example for other CWDM channels, the minimum required receiver input power as a function of the transmission distance for the 1551 nm VCSEL. The additional abscissa axes shows the large accumulated chromatic dispersion of 17 ps/nm.km for SSMF at 1.55 μm wavelength. For the receiver sensitivity measurements using the pin-receiver described in Section 2.5.1, the decision threshold as well as the sampling time were optimized manually. The curves were taken at $BER = 10^{-9}$ (square markers) for transmission without FEC and at $BER = 10^{-3}$ (circular markers). The laser driving conditions were optimized for maximum reach when measuring the solid curves, while the dashed curves represent the results for optimum driving conditions in the *back-to-back* (b2b) case. Curve a) in Fig. 3.2 shows a maximum power-limited reach of 65.6 km. Here, the average PRBS modulated laser output power was -0.95 dBm, and the overall fiber loss coefficient was 0.218 dB/km (dotted line). The improvement of sensitivity between 20 and 50 km is discussed in Section 3.1.3.

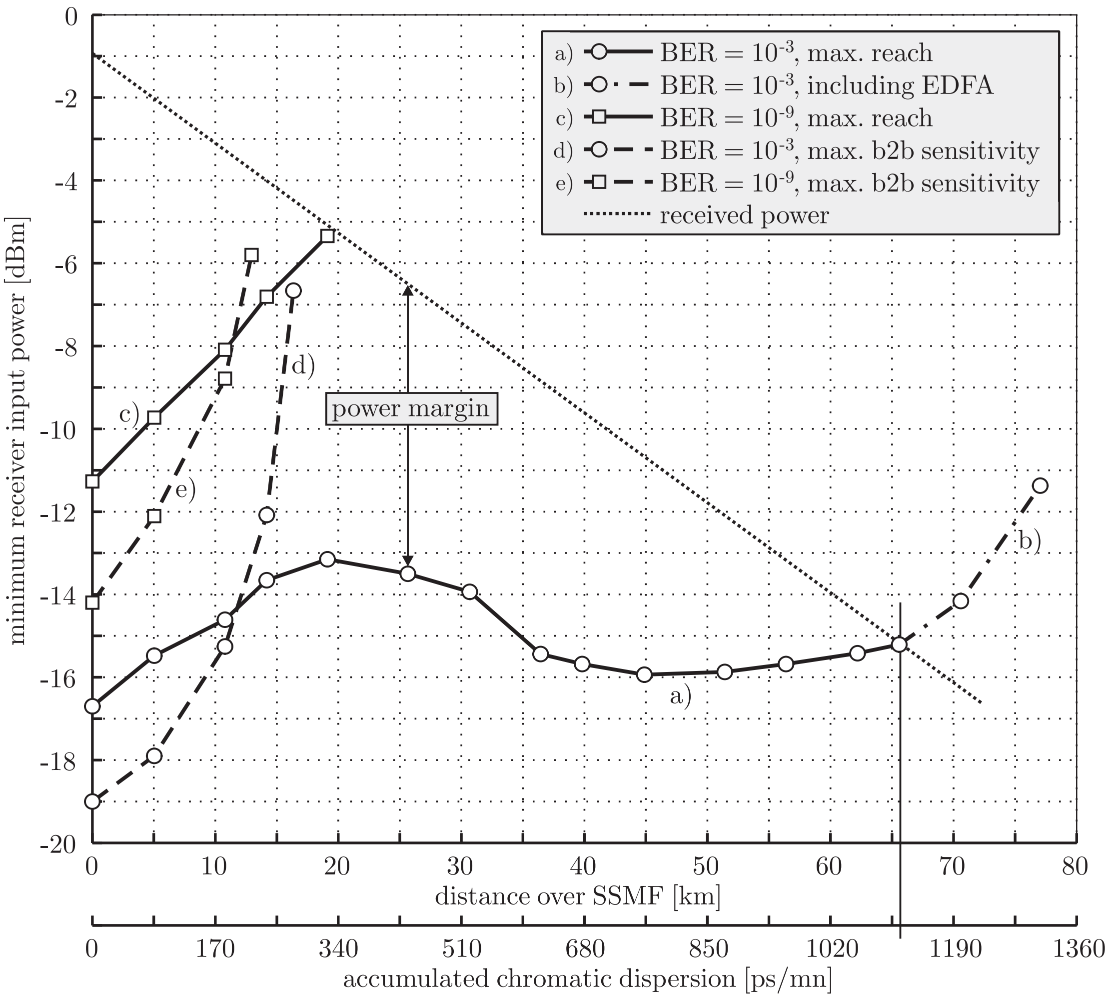

Figure 3.2: Minimum receiver input power versus transmission distance for the 1551 nm VCSEL with driving conditions optimized for maximum reach (solid lines) and for optimum back to back performance (dashed lines) at a data rate of 10.7 Gbit/s and at room temperature of $T = 23\,°$C. An EDFA was used in order to determine the dispersion limited link distance (dashed-dotted line).

To emulate a VCSEL of slightly higher output power, a 39 dB gain EDFA was placed at the output of the laser. So the dispersion-limited reach in Fig. 3.2b) was found to be around 77 km. The maximum reach for transmission without FEC at $BER = 10^{-9}$ was 19.2 km and is depicted in curve c). The dashed lines d) and e) were dispersion-limited at rather short reach because of their non optimal driving conditions, which are listed in Table 3.1. As one can see, good driving conditions for long distances are at a high bias current and a relatively low modulation voltage swing compared to optimal b2b conditions. Therefore, the resulting extinction ratio is low, but the impact of chirp, which could be adjusted via the driving parameters, plays a more important role.

curve	a)	b)	c)	d)	e)
bias current I_b	5.2 mA	5.2 mA	6.0 mA	4.4 mA	4.5 mA
modulation voltage V_{PG}	1.22 V_{pp}	1.22 V_{pp}	1.4 V_{pp}	2.0 V_{pp}	2.0 V_{pp}

Table 3.1: Driving conditions for the 1551 nm VCSEL used for measurements depicted in Fig. 3.2.

3.1.2 Benefits from FEC

The use of enhanced FEC highly relaxes the requirements concerning the BER and thus for the receiver sensitivity. Block-error free transmission is ensured when employing FEC, which is able to correct BERs of 10^{-3} to values below 10^{-15}.

A comparison of the solid curves in Fig. 3.2, which were taken at BERs of 10^{-3} and 10^{-9} clearly show the benefits from FEC. In the back-to-back case, a theoretically sensitivity gain of 5.5 dB (cf. Fig. 2.2b) was achieved. The larger the fiber distance, the more is the profit from FEC due to the impact of accumulated chromatic dispersion. While the transmission system without forward error correction was limited to a link length around 20 km, the system using FEC reached distances of three times more. Only FEC makes the receiver sensitivity improvement for a BER of 10^{-3} at distances between 20 km and 50 km usable, and thus enables the system to reach the dispersion limit around 77 km.

3.1.3 Interplay between chromatic dispersion and laser chirp

As depicted in Fig. 3.2a), the measured receiver sensitivity improved between 20 and 50 km of fiber distance. This was caused by the interplay of chromatic dispersion and adiabatic laser chirp. When operating the VCSEL at an increased bias current around 5.5 mA, the laser chirp acted advantageous on the propagation after an initial distance of 20 km. This transmission behavior is known as the *self-steepening effect* [19].

There are two components of chirp. The transient chirp mainly appears at modulation slopes and describes the wavelength dependency in the non stationary state of the laser, while the adiabatic chirp is of static nature and results from a change of the refraction index due to various laser current. In this considered case, the transient component of the chirp played an unimportant role, because of the poor extinction ratio of 4 dB, which can be obtained from Fig. 3.3, and resulted from the high bias current. The optical spectrum is strongly governed by the remaining adiabatic component of the chirp. As it is shown in Fig. 3.3, which depicts the optical back-to-back frequency spectrum at the driving conditions for maximum reach, the "zero"-states of the optical pulses produce a peak at lower frequencies of the spectrum, compared to the "one"-states, which generate a peak 6.9 GHz above. The dispersion of the signal at 1551 nm in SSMF accelerates the high frequencies and slows down the low frequencies. Therefore, the "one"-states propagate faster than the "zero"-states within a certain amount of fiber. This leads to pulses with a higher intensity spike at the rising edge and a tail at the end of the pulse, which means a recompression of the pulses and therefore a wider eye opening.

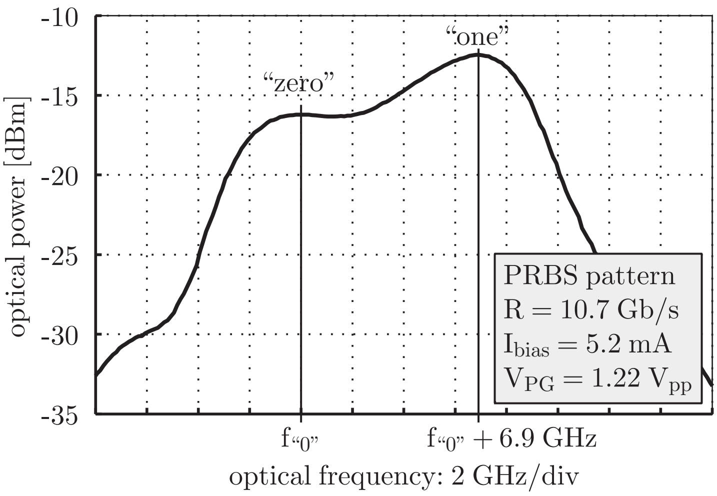

Figure 3.3: Optical frequency spectrum at driving conditions for curve a) of Fig. 3.2.

The eye diagrams and the bit sequence in the pattern diagrams of Fig. 3.4 show the characteristic behavior described above. After an initial propagation over 20 km of fiber, the influence of dispersion seemed to limit the bandwidth for the part of the pattern consisting of a "0101" bit sequence. At a distance around 40 km, the overshoots at the rising edge of the pulses compensated the "bandwidth limitation" and the logical states appeared more pronounced. This lead to a better receiver sensitivity. For distances greater than 65 km the overshoot got visible also in the eye diagrams and it started shifting to the original "zero"-states. This overlapping lead to eye closure and a rapid performance degradation. At distances around 75 km, this effect caused the dispersion limitation of the system.
All electrical measurements for Fig. 3.4 were done at the same scale. So they also illustrate the different minimum signal magnitudes required at the receiver to achieve a BER of 10^{-3}.

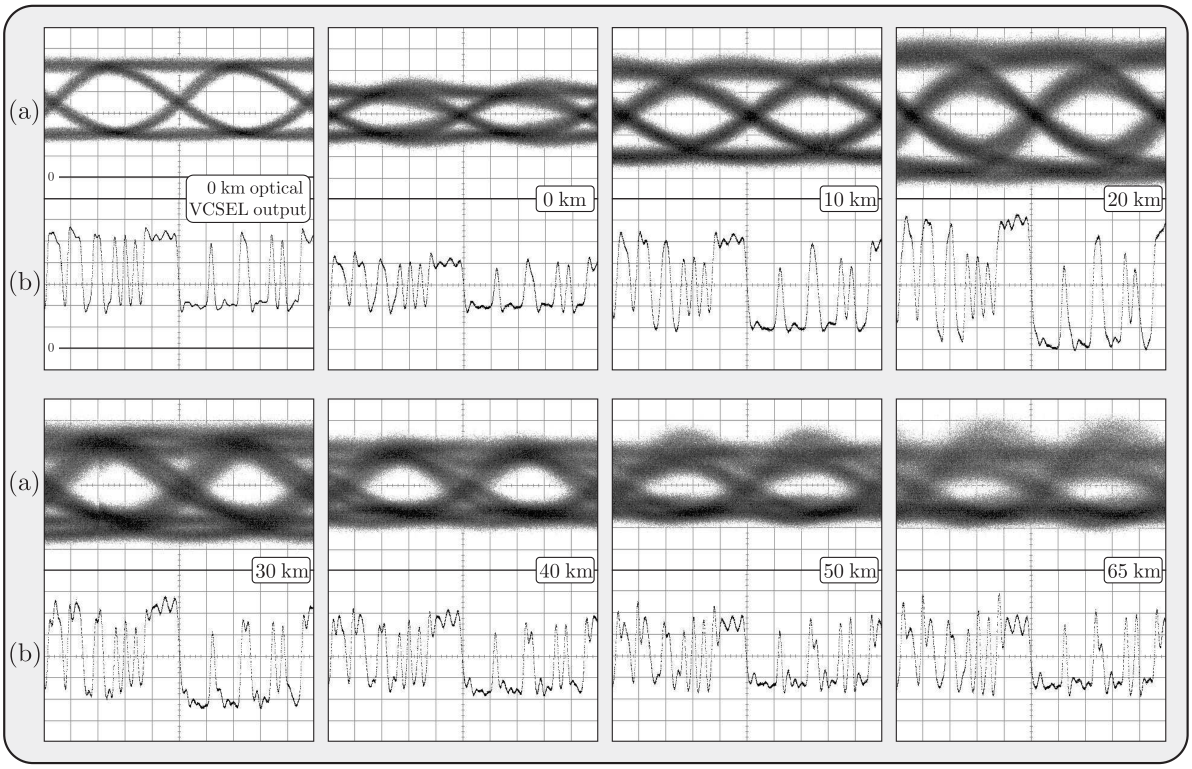

Figure 3.4: Received electrical (a) eye diagrams and (b) pattern diagrams for $BER = 10^{-3}$ after propagation over a certain amount of fiber at a wavelength of 1551 nm. The first pair of diagrams illustrates optical back-to-back behavior.

3.1.4 Comparison to DFB-laser system

Figure 3.5 depicts the pin-receiver sensitivity versus the distance over SSMF for the single channel transmission system described above as well as for a similar transmission system that used a directly modulated DFB-laser as transmitter [20]. Both systems operated at a data rate of 10.7 Gb/s and a BER of 10^{-3}. The main difference was just the laser source. As one can see, the behavior is in principle the same, but in the DFB system, the distinction of the self-steepening effect was more and the dispersion limited reach was some 10 km less.

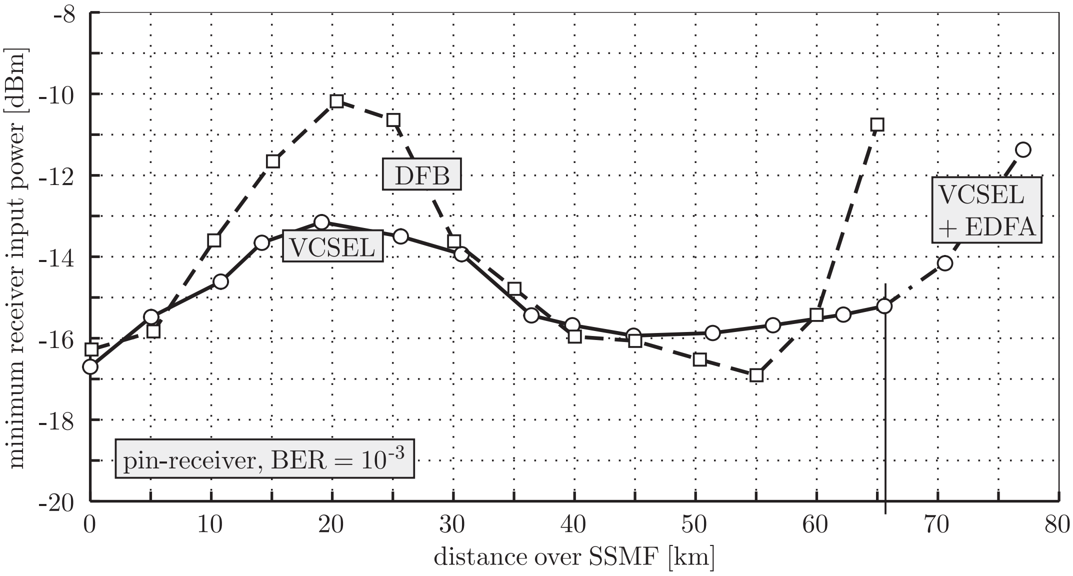

Figure 3.5: Comparison of receiver sensitivity of VCSEL and DFB-laser based transmission systems at 10.7 Gb/s [20].

3.2 Multiple channel transmission system

The setup of the CWDM system demonstrated in this work is depicted in Fig. 3.6(a) and the corresponding photo of the setup is presented in Fig. 3.7. The CWDM system employed four uncooled VCSELs operating at a wavelength from 1531 to 1591 nm and which were driven with a PRBS pattern of length $2^{31} - 1$, using *non-return-to-zero* (NRZ) modulation at the FEC data rate of 10.7 Gb/s.

Channel 1, including the Picosecond 5541A bias tee, was the main channel. It contained the VCSEL of the actually measured wavelength and was modulated by the *data* output of the pattern generator. The three other VCSELs were modulated by the remaining $\overline{data}$ output, each with optimized driving conditions for maximum reach. Various lengths of electrical cables and fiber pigtails ensured different data traffic for all channels on the common SSMF, because of the short bit duration of 93 ps, corresponding to a bit length of approximately 20 mm. The value of the 4 dB attenuator was adapted for certain cases to meet the optimal driving voltage swing of all four lasers. Figure 3.6(b) shows the supply of negative bias current to the VCSELs via conventional DC-power supplies. The voltage splitter combined with the laser diode limited the maximum current and the additional capacitor built a low pass filter with a large time constant of 0.13 s that absorbed possible surges, which could be caused by voltage transients on the power line.

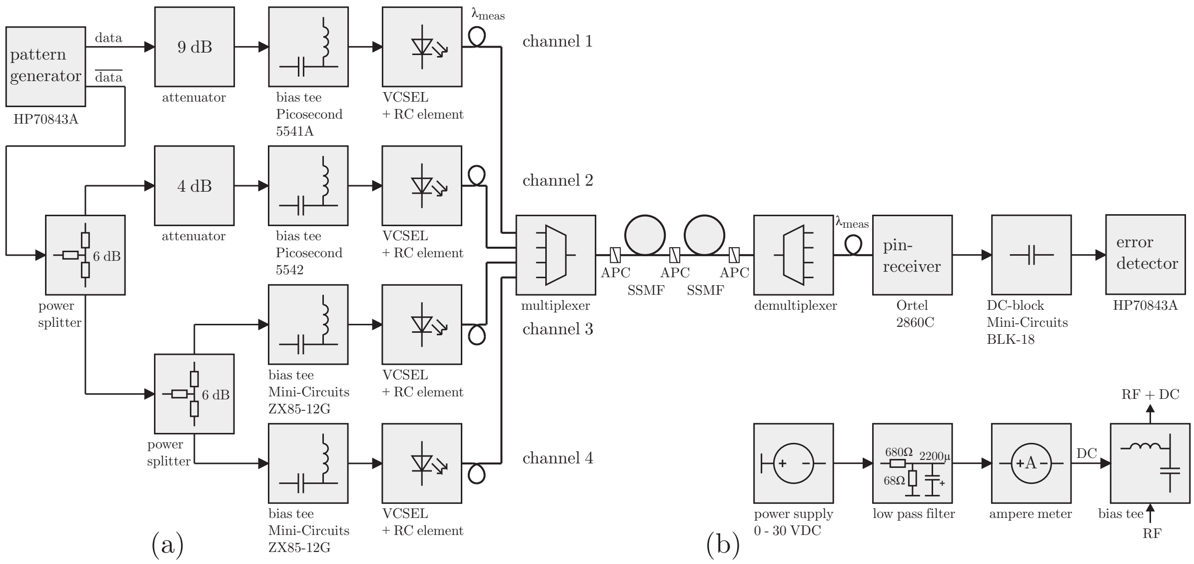

Figure 3.6: (a) Setup of 4-channel CWDM system and (b) surge protected supply of bias current.

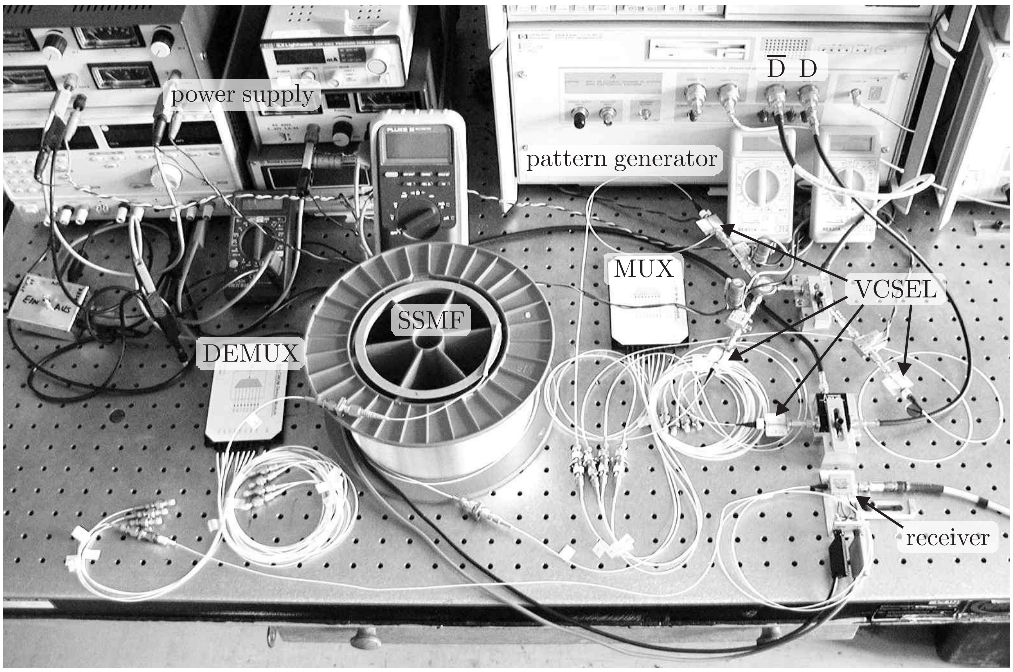

Figure 3.7: Setup of the 4-channel CWDM system.

3.2.1 4-channel unidirectional system

The setup in Fig. 3.8(a) depicts the principle of a 4-channel unidirectional CWDM system. All four VCSELs were driven simultaneously at conditions for maximum reach. Figure 3.8(b) shows the CWDM spectrum of the unmodulated VCSELs as launched into the SSMF at room temperature. The power coupled to the fiber differed by at most 1.3 dB from channel to channel. The spectral lines beside the laser wavelengths and below −60 dBm were caused by nonlinear behavior of the multiplexer and resulted from the spectral line of the upper adjoining channel. But this effect did not have any impact on the system performance.

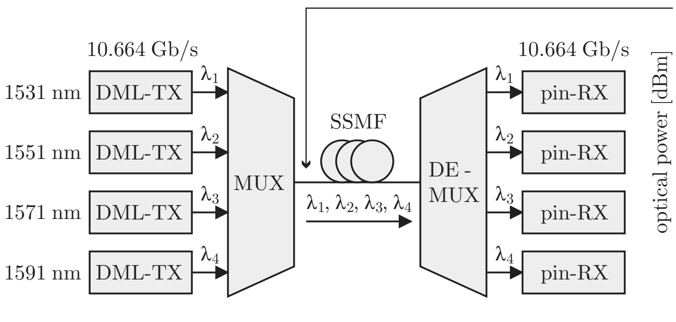

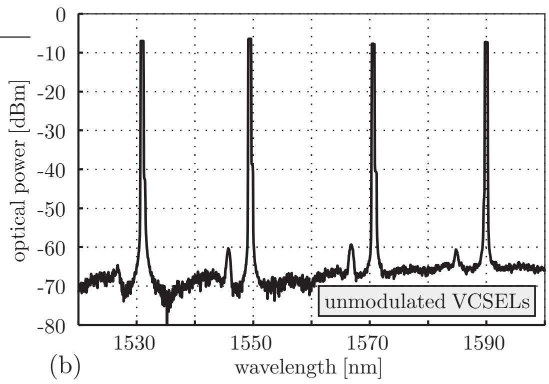

Figure 3.8: (a) Principle of the 4-channel unidirectional CWDM transmission and (b) CWDM spectrum launched into the fiber.

The sensitivity measurements were done at a BER of 10^{-3} in order to use enhanced FEC, which should ensure a maximum final BER of 10^{-15} for block-error free transmission. Several measurement results for each individual channel in the overall CWDM systems are presented in Fig. 3.9. It depicts the pin-receiver sensitivity for the maximum transmission distance over SSMF as well as the sensitivity for back-to-back operation, all with driving conditions optimized for maximum reach (see Table 3.2) to demonstrate full functionality without the need for dynamic laser reconfiguration. The measured points with open markers were done at room temperature $T = 22\,°\mathrm{C}$, while the marker "×" represents the 1591 nm channel, where the VCSEL operated at an elevated ambient temperature of 65 °C.

The lines in the figure are "power"-curves and illustrate the loss along the optical fiber of $\alpha_T = 0.2\,\mathrm{dB/km}$. The length of the arrows, which point to the measured receiver sensitivities at maximum reach, represent the constant insertion loss A_0, that results from the multiplexer, the demultiplexer, and connectors.

At room temperature, the best performing channel was found at a wavelength of 1551 nm with a reachable distance of 52 km. The worst performing channel at 1591 nm wavelength resulted in a reachable distance of 45 km, due to an increased insertion loss of the demultiplexing filter at long wavelength (cf. Table 2.4). All channels were loss limited. This means that the laser with the poorest characteristic or the thin film filter with the highest insertion loss limit the reach of the overall system. A possible selection process when purchasing the components could significantly enhance the reach of the overall CWDM system.

To demonstrate the performance at increased ambient temperature, the VCSEL of the worst performing channel at 1591 nm, was heated to 65 °C. As one can see from Fig. 3.9, its optical power decreased by 2.3 dB. This reduction did not totally result from the laser's thermal characteristics. After a cool down to room temperature, the VCSEL's threshold current left unchanged, but its coupling to the SSMF declined non reversible. Nevertheless, a maximum distance of 25.6 km could be reached, when operating the VCSEL at 65 °C.

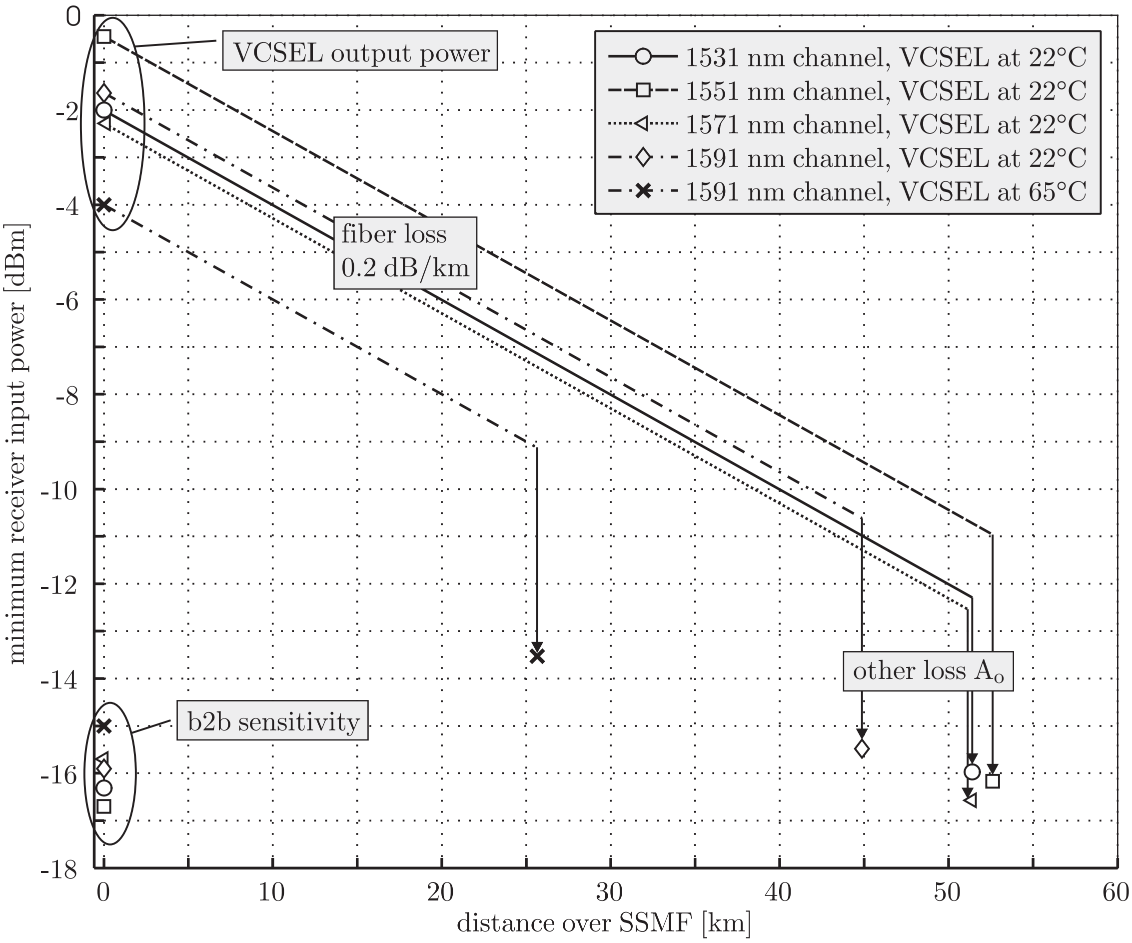

Figure 3.9: Minimum receiver input power versus transmission distance for the unidirectional CWDM system with driving conditions optimized for maximum reach at a data rate of 10.7 Gbit/s and a BER of 10^{-3}.

channel	1531 nm	1551 nm	1571 nm	1591 nm	1591 nm at 65 °C
bias current I_b	4.4 mA	6.0 mA	6.0 mA	7.5 mA	7.5 mA
modulation voltage V_{PG}	1.8 V_{pp}	1.5 V_{pp}	1.5 V_{pp}	1.8 V_{pp}	1.4 V_{pp}

Table 3.2: Driving conditions for the VCSELs, according to Fig. 3.9.

3.2.2 4-channel bidirectional system

The bidirectional CWDM experiment included a wavelength partitioned system with four interleaved channels, where two channels propagated in each direction as depicted in Fig. 3.10. All four VCSELs operated at a room temperature $T = 25\,°C$, and were modulated simultaneously at driving conditions optimized for maximum reach.

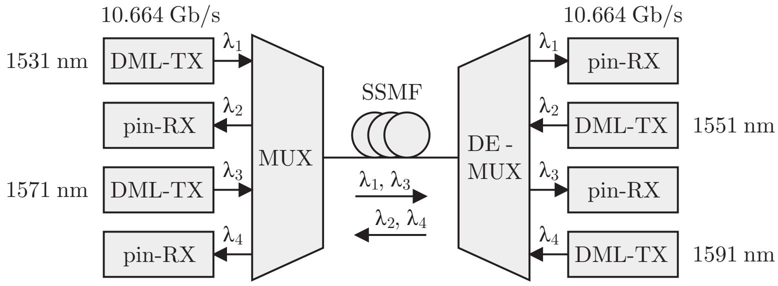

Figure 3.10: Principle of the 4-channel interleaved CWDM transmission.

The receiver sensitivity measurements were done at a BER of 10^{-3}. The results are listed in Table 3.3. During the measurements, only marginal differences of less than 0.1 dB occurred, when compared to the results of the unidirectional CWDM system.

For each channel, the input power into the fiber was approximately −7 dBm (cf. Fig. 3.8b) due to the insertion loss of the multiplexer and the connectors. Therefore nonlinear effects in the fiber were negligible. Turning off neighboring channels did not result in any changes of the receiver sensitivity, which indicated negligible crosstalk.
The total CWDM transmission capacity for this system is given by

$$C_T = N_{CH} \cdot R_{CH} \cdot L = 1.8\,\mathrm{Tb/s}\cdot\,\mathrm{km}, \tag{3.1}$$

where N_{CH} is the number of channels, R_{CH} is the channel data rate, and L is the maximum reach of the whole CWDM system.

channel	maximum distance L	back-to-back receiver sensitivity S_{b2b}	average VCSEL output power P_o	receiver sensitivity at max. distance S_L
1531 nm	51.4 km	−16.3 dBm	−2.01 dBm	−15.97 dBm
1551 nm	52.6 km	−16.7 dBm	−0.45 dBm	−16.17 dBm
1571 nm	51.4 km	−15.7 dBm	−2.28 dBm	−16.57 dBm
1591 nm	44.9 km	−15.9 dBm	−1.64 dBm	−15.48 dBm

Table 3.3: Results of bidirectional CWDM experiment for $BER = 10^{-3}$ at room temperature $T = 25\,°\mathrm{C}$.

3.3 Conclusion

In this work, a bidirectional 4-channel CWDM transmission over standard single-mode fiber was experimentally demonstrated. The transmission system was based on commercially available, non preselected, uncooled long wavelength VCSELs from 1531 to 1591 nm, which were directly modulated at a bit rate of 10.7 Gb/s in order to enable forward error correction. All four channels were transmitted over a loss-limited link distance of more than 45 km, without any kind of optical or electronic dispersion compensation.

Also the *self-steepening effect*, that occurred at special driving conditions of direct modulated lasers after signal propagation over an initial amount of fiber, and its advantageous for the receiver sensitivity, were shown.

In future research projects related to this work, it would be interesting to address the following topics:

- The use of an *avalanche photodiode* (APD) receiver instead of a pin-receiver yields to a sensitivity gain of typically 7 dB (see section 2.5.2) and therefore especially loss-limited systems profit due to an increased link distance.
- To setup a CWDM system including VCSELs with a higher optical output power in order to reach the dispersion limit, and with an improved packaging for optimized RF-behavior, or 10 Gb/s rating.
- A performance demonstration of a forward error correction unit together with the use of *electronic dispersion compensation* (EDC) might enhance sensitivity and reachable distance, especially in the case of high dispersion [7].
- A detailed analysis of the self-steepening effect and its impact on the performance of a transmission system as well as its chances and limits to increase the reachable link distance.
- A detailed cost-performance analysis for optical access networks like *fiber-to-the-home* (FTTH).

Part II

Free-space wavelength diversity

Chapter 4

Compensation of the influence of atmospheric turbulence

Free space optics (FSO) is an emerging technology which allows for broadband communications in an unlicensed frequency range. Due to the small optical wavelength, high antenna gains of telescopes are used to establish *line of sight* (LOS) communication links with small laser beam diameters and low divergence. The field of FSO applications reaches from terrestrial to inter satellite laser links. When the laser beam propagates through the atmosphere, the influence of turbulence degrades the ideal gaussian laser beam.

In this part of my diploma theses, I focus on the possibility of wavelength diversity, to partly compensate the influence of turbulent atmosphere.

4.1 Motivation and overview

Figure 4.1 shows various optical communication link scenarios, that are influenced by the turbulent atmosphere. It depicts a short building-to-building link with typical path lengths of up to some kilometers, which are usually influenced by strong turbulence in urban regions.

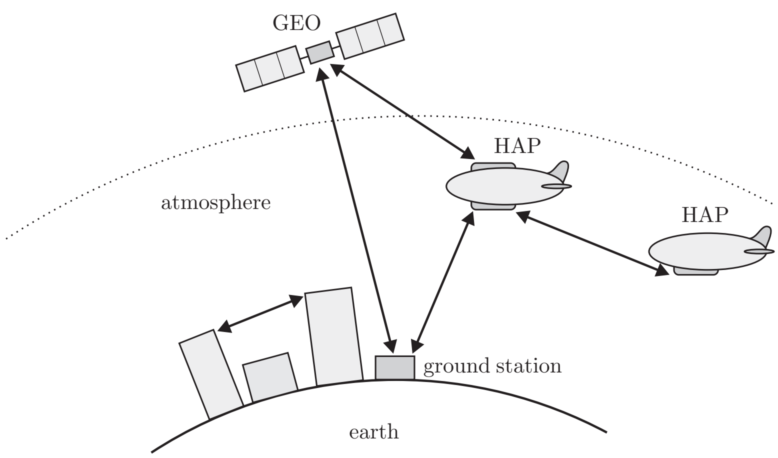

Figure 4.1: Optical communication link scenarios between ground station, *high altitude platforms* (HAPs), and GEO-satellite with beam propagation through the atmosphere.

Future FSO-links may as well supply *high altitude platforms* (HAPs)[1] with broadband data access. Another important link scenario is the communication between satellites and a ground station. Here, especially the up-link to a geostationary satellite, with a path length in the range from 36000 to 39000 km, is significantly more influenced by the atmosphere, compared to the down-link, due to the so called *shower curtain effect* [21].
The main effects of the turbulent atmosphere are [22]:

- attenuation – a loss of power due to absorption and scattering,
- beam wander – a time dependent statistical beam deflection (cf. Fig. 4.2a),
- beam spread – additional beam broadening compared to the diffraction limit, and
- scintillation – phase distortion causes interference within the beam and therefore variations in the intensity of the beam profile (cf. Fig. 4.2b).

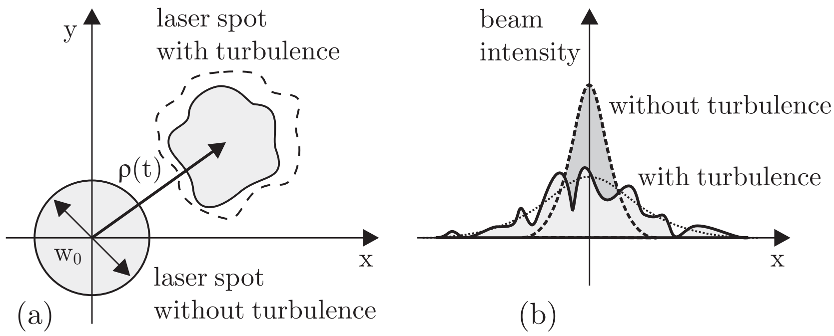

Figure 4.2: Atmospheric influence on the received beam: (a) time-dependent deflection leads to beam wander. (b) the originally gaussian beam (dashed line) keeps its whole intensity, but broadens (thin gaussian curve describes beam spread) and its intensity profile fluctuates (solid line describes scintillation) because of interference effects within the beam.

The fluctuation of the received laser beam is the result of small variations of the refraction index n_{atm} in the atmosphere due to changes of the local temperature T and the pressure p in the air flow. This can be considered as time-dependent, statistical arranged lenses of different sizes. An expression for the dependency of the refraction index is

$$n_{atm} = 1 + 77.6 \cdot 10^{-8} \left(1 + \frac{7.52 \cdot 10^{-15}\,\mathrm{m}^2}{\lambda^2}\right) \frac{p}{T} \quad \frac{\mathrm{m\,s^2\,K}}{\mathrm{kg}}, \tag{4.1}$$

where λ is the wavelength of the laser beam [23]. According to (4.1), the wavelength dependency is very small. However, the difference of the refraction index is $1.0 \cdot 10^{-7}$ for $T = 300\,\mathrm{K}$, $p = 1\,\mathrm{bar}$ and $\lambda_{1,2} = 1500/1600\,\mathrm{nm}$. This possibly allows for wavelength diversity. There exists a lot of theory for modeling the atmospheric behavior, but I focused my work primary on practical experiments.

[1]HAPs are unmanned aerial vehicles which are positioned at altitudes between 10 and 20 km.

In most cases, the turbulence broadens the laser beam by a multiple of its diffraction limit. If the diameter of the beam gets larger than the aperture of the receiving telescope, only a part of the transmitted power can be coupled to the receiver. Thus, the time-dependence of the received optical power leads to signal fading and an increased BER. The responsible effects are beam wander and scintillation. While beam wander can be compensated by the use of fast tracking mechanisms, scintillation is the remaining problem for FSO-links.

Beside the possibilities of adaptive optics or multi-beam illumination (space diversity) to minimize the influence of scintillation, I investigated wavelength diversity or multiple wavelength illumination in the wavelength range around 1.55 μm [24]. I used the long wavelength *vertical cavity surface emitting lasers* (VCSELs) from the CWDM system, described in Part I of this work, as transmitting laser source. They offer the possibility to be boosted by an *Erbium doped fiber amplifier* (EDFA), and this allows for low power consumption, which is important especially in FSO for satellite terminals.

4.2 Experiments at 633 nm wavelength

My first experiments were conducted at the visible wavelength of 633 nm. Figure 4.3 principally depicts the experimentally setup. The beam of a continuous wave (CW) HeNe-laser was coupled to the transmit telescope, which consisted of a flat secondary mirror and a concave primary mirror, with a focal length of 90 cm and a diameter of 20 cm. To double the optical path length, the laser beam was reflected via a flat mirror and finally projected to a diffusing screen. So the over all folded distance was 80.6 m. The laser beam was adjusted to be paraxial and its average $1/e^2$-diameter w_0 was measured to be 37 mm.

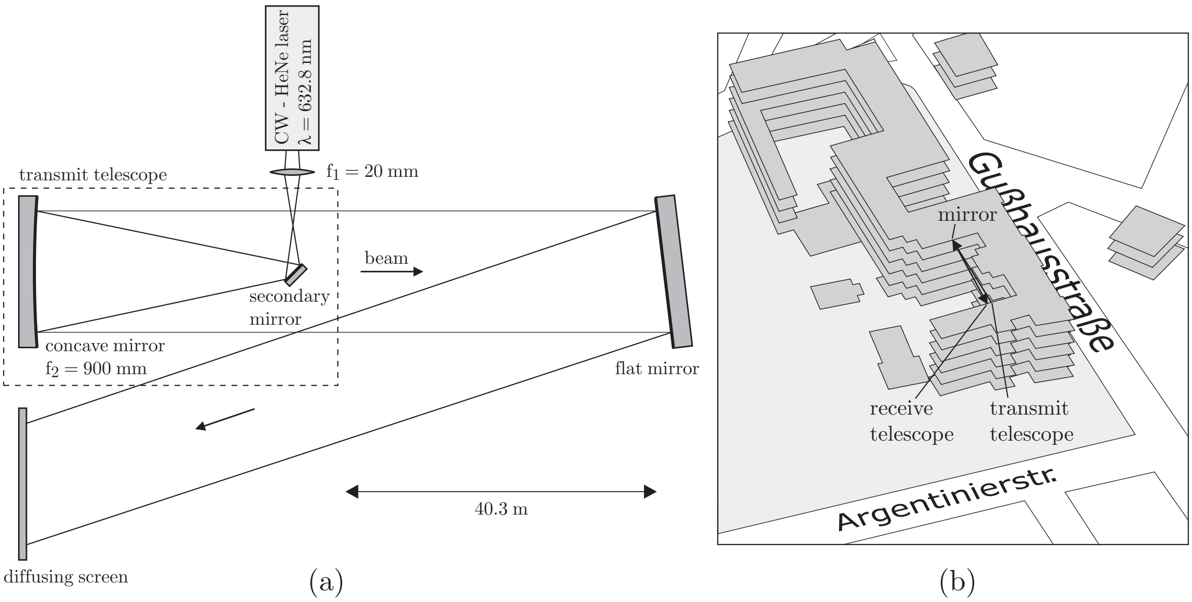

Figure 4.3: (a) Principal test setup for turbulence measurement and (b) path of laser beam propagation (Gußhausstraße 27–29, 1040 Vienna).

Figure 4.4(a) depicts the transmitted laser beam, which approximately had a gaussian intensity profile. Parts (b)–(j) of Fig. 4.4 show a picture series of intensity distributions of the received beam, captured in time intervals of 0.5 s, and with a short exposure time of 10 ms to avoid an averaging effect of the fast intensity fluctuations. As one can see from the photographs, even for this short propagation path, a pronounced scintillation effect was observable, but there was no significant beam wander recognizable. Only long term observation in the range of hours lead to beam wander due to thermal expansion of the buildings.

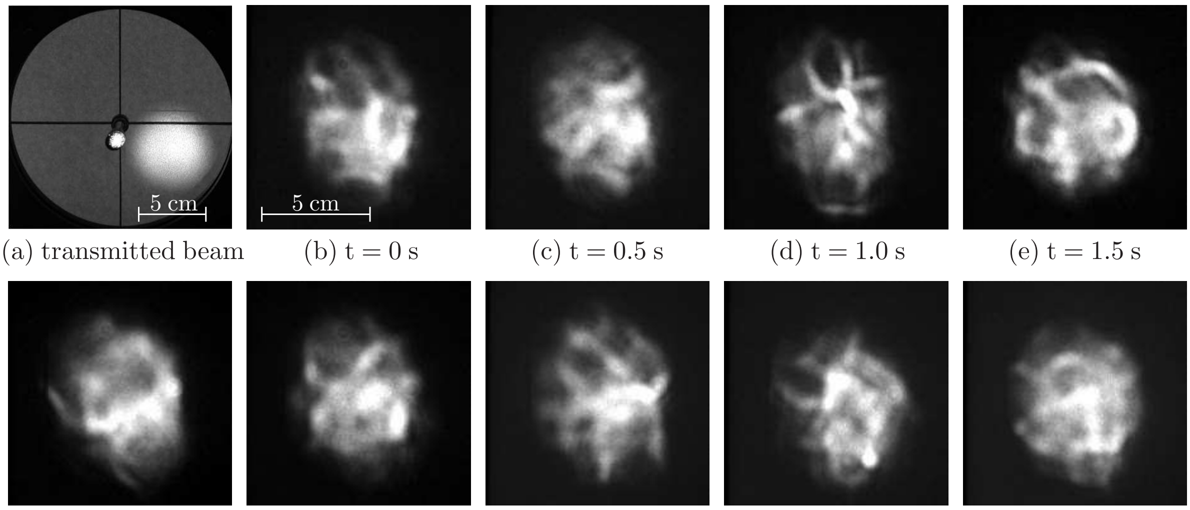

(a) transmitted beam (b) t = 0 s (c) t = 0.5 s (d) t = 1.0 s (e) t = 1.5 s

(f) t = 2.0 s (g) t = 2.5 s (h) t = 3.0 s (i) t = 3.5 s (j) t = 4.0 s

Figure 4.4: A series of snapshots of the laser beam after 80.6 m propagation demonstrates the influence of scintillation. The pictures were taken with an exposure time of 10 ms on 29$^{\text{th}}$ June 2006, 13:30 h, at cloudy weather, and at an air-temperature of 21 °C.

4.3 Experiments at 1550 nm wavelength

After successful demonstration of scintillation at the visible wavelength of 633 nm in the previous Section 4.2, I observed a very similar behavior at the wavelength of 1550 nm. This was done by using a CCD-video camera, which was sensitive in the infrared wavelength region. In this section, I present the results of multiple wavelength illumination for two different wavelengths around 1550 nm with a spacing of 60 nm.

4.3.1 Measurement setup

Figure 4.5(a) shows the measurement setup and Fig. 4.6(a) depicts the corresponding photograph. Two wavelengths were observed simultaneously to ensure the same turbulence for each of them. In the setup, a 1531 nm and a 1591 nm VCSEL were pulsed with a 10 kHz rectangle signal and a duty-cycle of 0.5. This was done in a synchronized way, so that the lasers turned on and off alternately. The two different wavelengths of the pigtailed VCSELs were then combined via a thin film multiplexer. This ensured a very good alignment of the two wavelengths within the common single-mode fiber. The coupling of the optical signal from the fiber to the transmit telescope was done via a microscope objective (see Fig. 4.6b). After beam propagation over the folded distance of 80.6 m, the whole laser beam illuminated a InGaAs pin-diode via an additional receive telescope. The diameter of the aperture in front of the receive telescope could be adjusted, so it was possible to select a part of the received laser beam to analyze its power variance. The power measurement was realized via a voltage measurement at the resistor in parallel to the photodiode, so optical power fluctuations could be observed on an oscilloscope.

Figure 4.5(b) illustrates a simple principle of linear optical power measurement via photodiode and oscilloscope. Illumination of the pin-diode causes a vertical shift of its current vs. voltage characteristic. To keep operation in the linear region of the diode's characteristic – the diode acts as current source – the voltage drop V_d at the pin-diode has to be chosen smaller than 0.2 V. The maximum expected received optical power $P_{o,max}$ was in the range of 0.1 mW and the spectral sensitivity S of the photodiode was 0.9 A/W, so the resistor should take values smaller than

$$R \leq \frac{V_d}{P_{o,max} \cdot S} = \frac{0.2\,\mathrm{V}}{0.1\,\mathrm{mW} \cdot 0.9\,\mathrm{A/W}} = 2222\,\Omega. \tag{4.2}$$

I chose a value of 1 kΩ. This resistor R together with the capacitance C_c of the coaxial cable to the oscilloscope form a low pass filter with the upper cut off frequency

$$f_u = \frac{1}{2\pi R C_c} = \frac{1}{2\pi \cdot 1\,\mathrm{k\Omega} \cdot 200\,\mathrm{pF}} = 795\,\mathrm{kHz}, \tag{4.3}$$

and therefore the bandwidth of the receiver system was sufficient highly for the 10 kHz modulation frequency of the VCSELs.

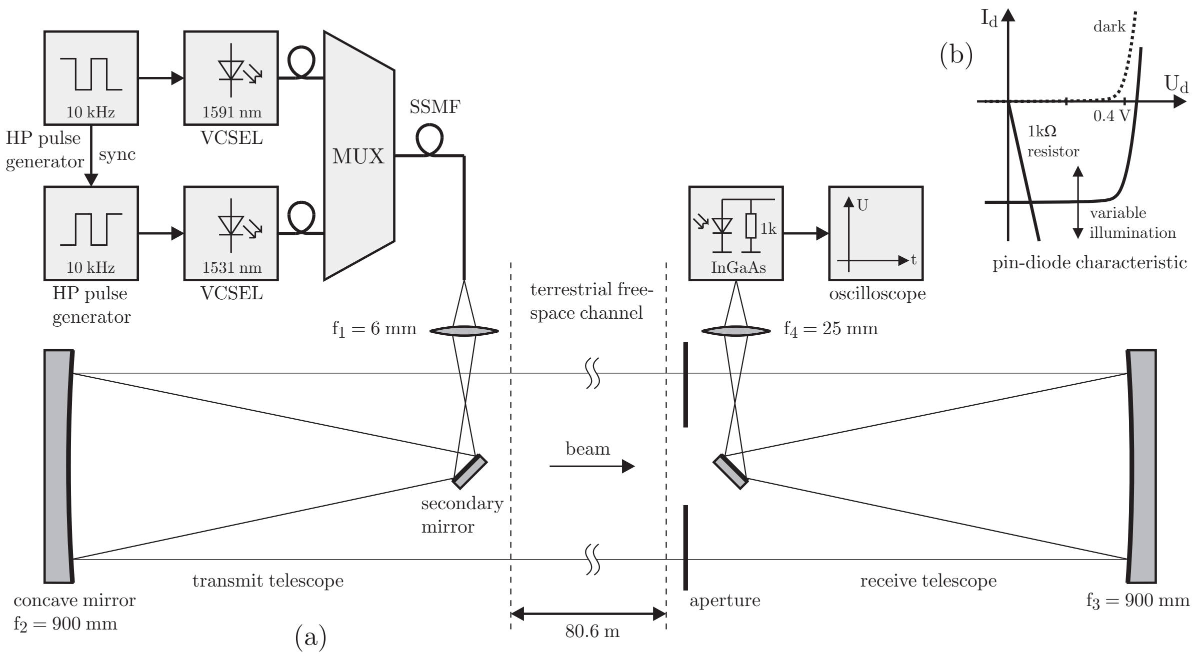

Figure 4.5: (a) Setup of the wavelength diversity experiment at 1531/1591 nm and (b) current vs. voltage characteristics of pin-diode for various illuminations. The photodiode acts as ideal current source for voltage drops below 0.2 V.

The average $1/e^2$ beam diameter w_0 for this experiment was 37 mm and the peak optical power of both wavelengths, which was measured at the output of the SSMF, was 160 μW while the received power at the pin-diode was 89 μW. Assuming no atmospheric absorption for this short link and a reflection coefficient of 4 % per surface of the three lenses (the microscope objective has two lenses) in the setup, the reflection coefficient of each of the 5 remaining mirrors becomes 0.934.

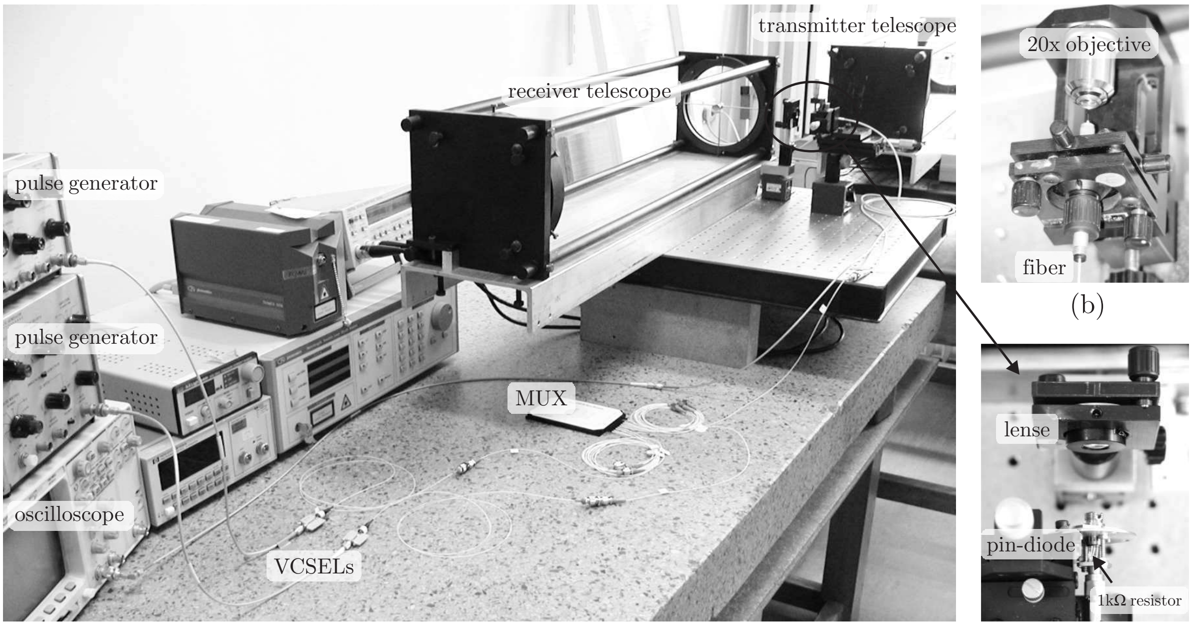

(a) (c)

Figure 4.6: (a) Setup of the wavelength diversity experiment at 1531/1591 nm and (b) coupling of optical signal from SSMF to the transmit telescope. (c) The coupling of the received beam to the pin-diode required an additional lense, because of the small sensitive region with a diameter of 100 μm.

4.3.2 Results for wavelength diversity experiment at 1531/1591 nm

In Fig. 4.7, the results of the diversity experiment at 1531/1591 nm are depicted. All diagrams show the received optical power versus time, at a scale of 1.11 μW/mV for both wavelengths.

Figure 4.7(a) illustrates the rectangular modulation of the 1591 nm VCSEL at a frequency of 10 kHz, while Fig. 4.7(b) depicts the situation for both VCSELs, where the 1531 nm VCSEL was driven for a slightly lower output power. The lasers turned on alternately, which resulted in separate lines for the different wavelengths in Fig. 4.7(c)[2]. The first three diagrams were taken without an aperture in front of the receive telescope, so the total laser beam illuminated the pin-diode, and thus the received power was constant in spite of scintillation. Figures 4.7(d)–(f) show the fading of the received power for aperture diameters from 30 mm to 6.5 mm. Its bandwidth ranges up to a frequency of some 100 Hz. As one can see, the average received power decreases rapidly with smaller apertures, and the power variance grows, but there is

[2]It equals Fig. 4.7(b) with the exception of a slower time scale.

no wavelength dependency observable even for the smallest aperture. Both wavelengths were influenced by the turbulence of the atmosphere in the same way, and therefore, only small wavelength diversity could be achieved with the wavelength difference of 60 nm.

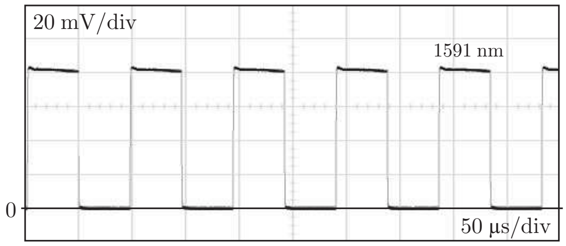

(a) no aperture, 1591 nm VCSEL modulated

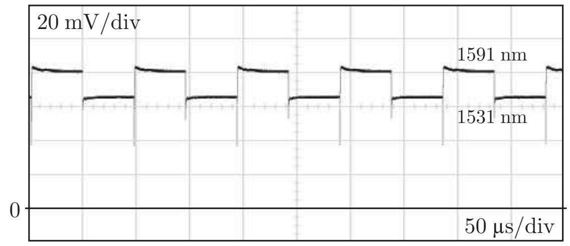

(b) no aperture, both VCSELs modulated

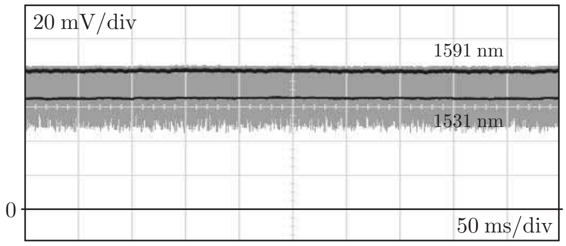

(c) no aperture, VCSELs modulated

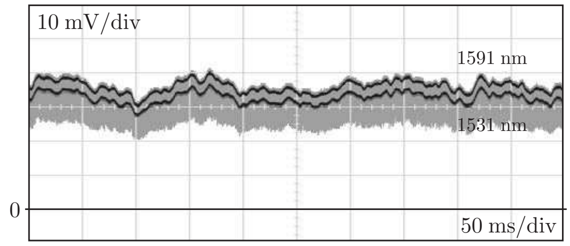

(d) aperture of 30 mm diameter

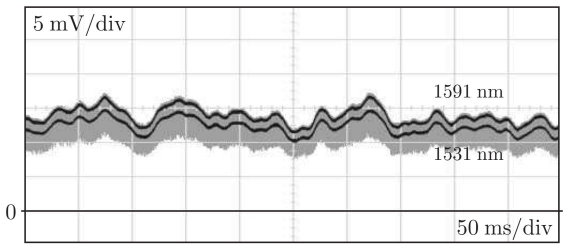

(e) aperture of 15 mm diameter

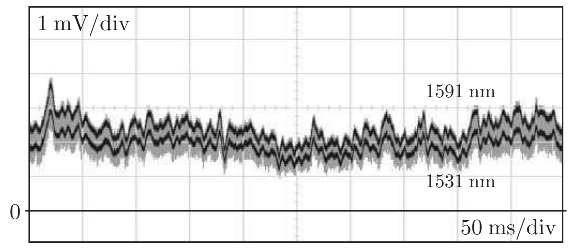

(f) aperture of 6.5 mm diameter

Figure 4.7: Received optical power vs. time at a scale of 1.11 μW/mV: (a) of the total laser beam for the 10 kHz pulsed 1591 nm VCSEL; (b) of the total laser beam for modulation of both VCSELs, where the 1531 nm laser was driven for lower output power; (c) at the same conditions as in (b), but slower time scale; (d) with an aperture of 30 mm diameter leading to moderate power variance; (e) with an aperture of 15 mm diameter; (f) with an aperture of 6.5 mm diameter leading to strong fading and low average power.

4.4 Experiments at large wavelength difference

Because of the negligible effect of wavelength diversity observed in the previous Section 4.3, a similar experiment was done at a larger wavelength spacing. In this section, I present the results of multiple wavelength illumination for two wavelengths at 633 and 1591 nm.

4.4.1 Measurement setup

Figure 4.8 illustrates the measurement setup for this wavelength diversity experiment, where I used a 1591 nm VCSEL and a CW-HeNe-laser source at a wavelength of 632.8 nm. The principle of measurement was similar to the experiment done in the infrared region, and the two wavelengths were observed simultaneously. The HeNe-laser could not be directly modulated. Thus its beam was chopped by a rotating, punctured disk (see Fig. 4.9), which lead to a modulation frequency of about 1 kHz. The chopped beam was coupled into a fiber and multiplexed with the 1591 nm signal via a 50/50 power splitter. I used single-mode fiber components for 1.5 μm, and thus, the red light of the HeNe-laser was not necessarily in its fundamental mode. The optical fibers were mechanically adjusted to realize an approximately gaussian beam profile at the transmit telescope. Tightening and fixing the fibers, avoided mode conversion of the red light during the measurements. The optical signal propagated over the folded distance of 80.6 m, until it was received by an InGaAs pin-diode. This photodiode had a reduced sensitivity of only 0.11 A/W at 633 nm. Thus, the optical output power of the two lasers was adjusted, in order to ensure comparable curves at the oscilloscope's display. The time averaged $1/e^2$ beam diameter w_0 for this experiment was 37 mm.

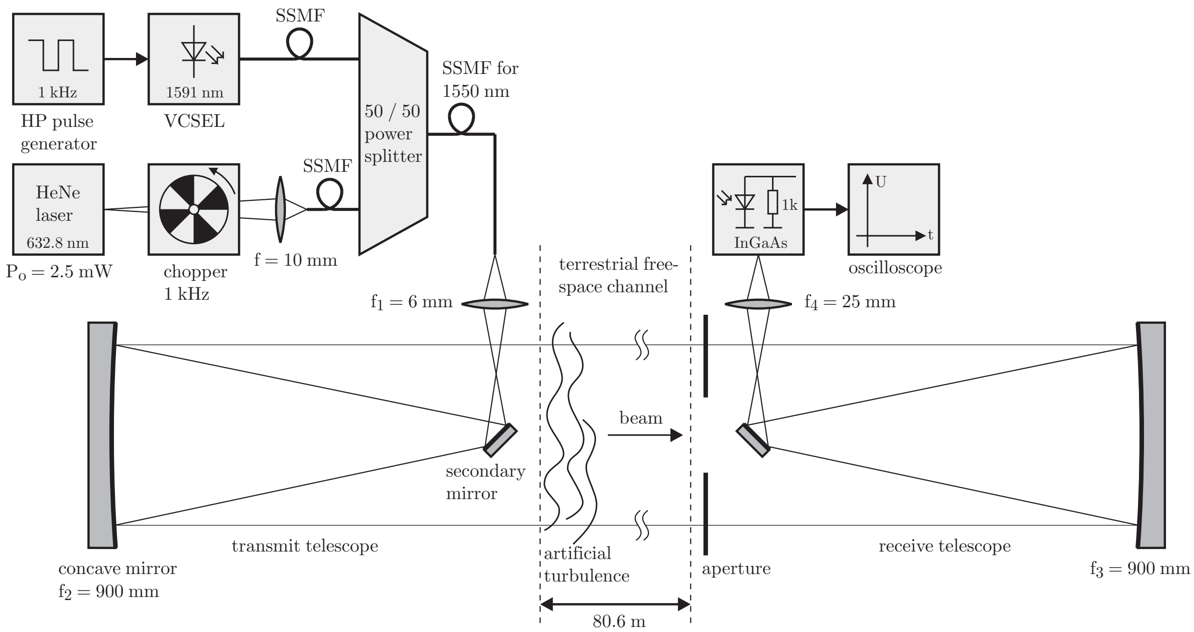

Figure 4.8: Setup for wavelength diversity experiment at 633/1591 nm. The laser beam propagated over a folded distance of 80.6 m with a $1/e^2$-diameter of 37 mm.

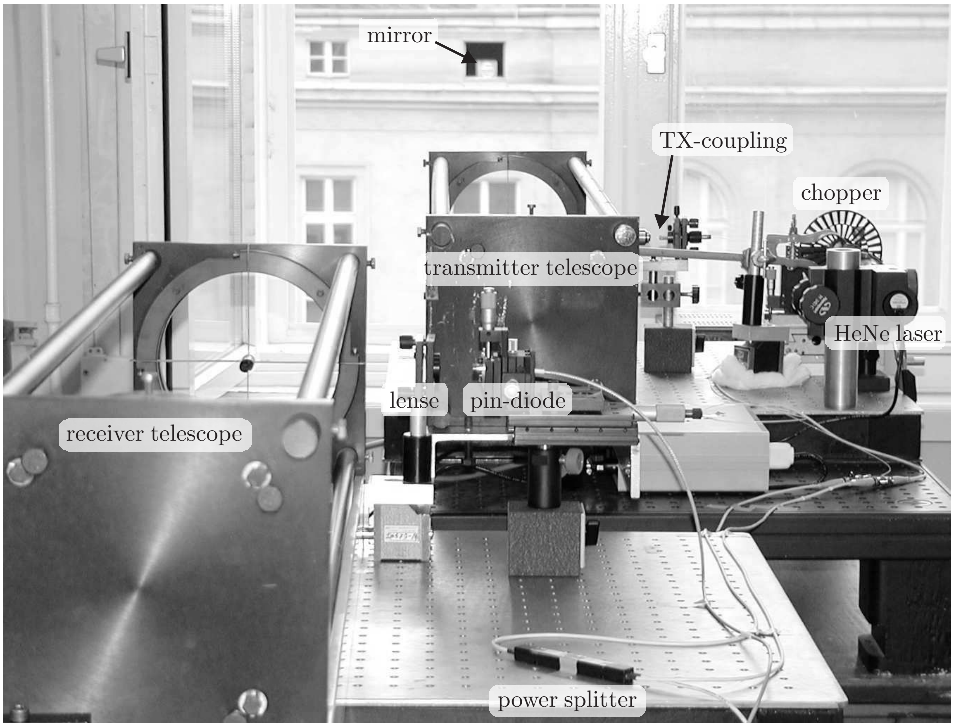

Figure 4.9: Setup for wavelength diversity experiment at 633/1591 nm. The photograph illustrates the folded propagation path including the mirror at the far end.

4.4.2 Results of terrestrial free-space experiment at 633/1591 nm

Figure 4.10 depicts the results of the diversity experiment at 633/1591 nm. All diagrams show the received optical power versus time at a scale of $1.11\,\mu$W/mV for the infrared wavelength, and $9.09\,\mu$W/mV for the red one. This experiment was done at an air-temperature of 23 °C and cloudy weather.

In Fig. 4.10, diagrams (a) and (b) illustrate the rectangle modulation of the 1591 nm VCSEL and the chopped beam of the HeNe-laser. Both signals were not synchronized and had a frequency of approximately 1 kHz, which was limited by the mechanic chopper. The superposition of the optical signals is depicted in Fig. 4.10(c). A variable overlapping of the pulses caused four different power levels, where only the two levels in the middle range were of interest, which represented the received power for each wavelength. The different scaled Fig. 4.10(d) demonstrates the case without aperture in front of the receiver, where the total beam was captured by the pin-diode, which yielded in a constant received power for each wavelength. Figures 4.10(e) and (f) finally present the influence of scintillation for aperture diameters of 15 and 6.5 mm. In spite of the large wavelength difference of a factor 2.5, the power versus time curves show only minimal wavelength dependency. Thus, the use of wavelength diversity in this scenario yields to negligible performance enhancement. Further on, such a large wavelength distance makes the practical use of multiple wavelength illumination with common optical components very difficult.

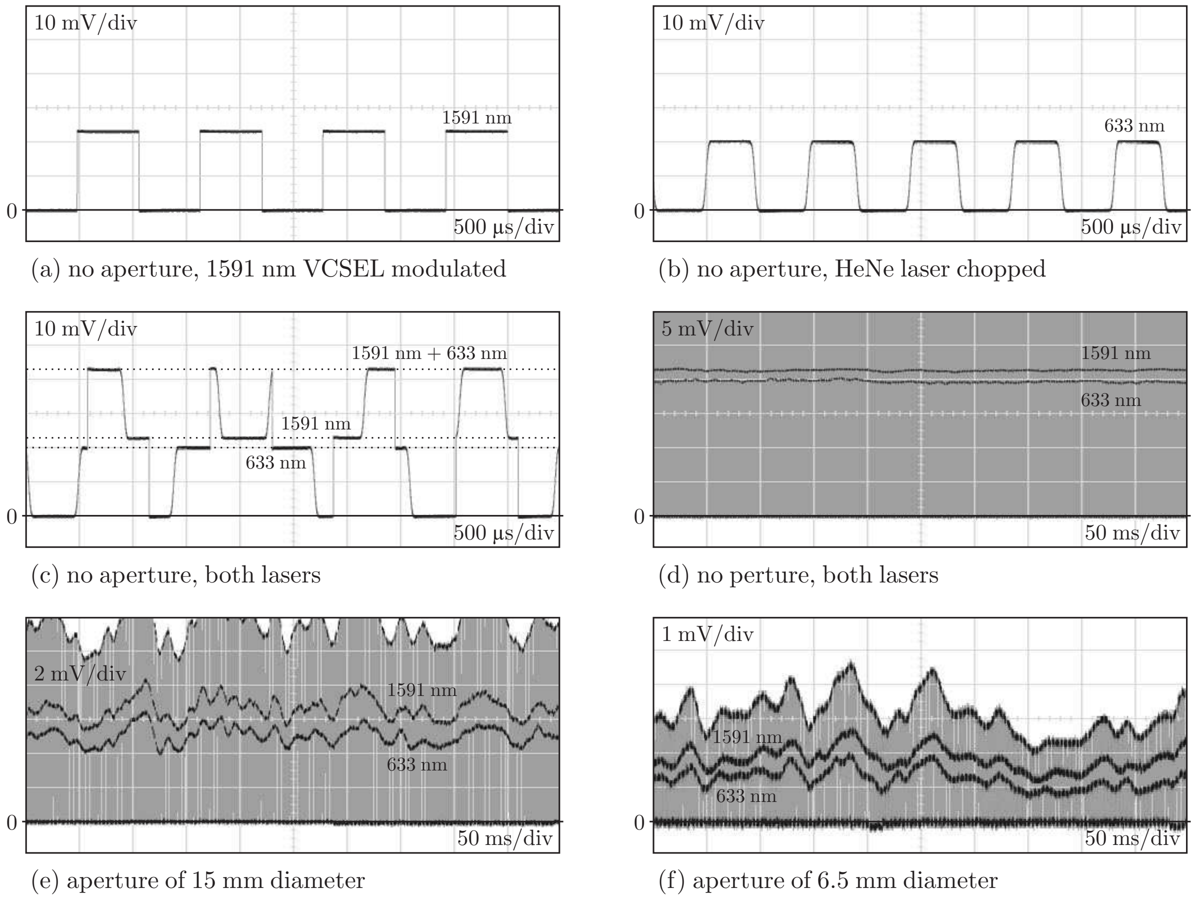

Figure 4.10: Received optical power vs. time, at scales of 1.11 μW/mV (1591 nm) and 9.09 μW/mV (633 nm) for a free space $1/e^2$ beam diameter of 37 mm: (a) of pulsed 1591 nm VCSEL without aperture at the receiver; (b) of 1 kHz chopped HeNe-laser without aperture; (c) of the totally received laser beam with modulation of both lasers at fast time scale; (d) at same conditions as in (c), but slower time scale; (e) with an aperture of 15 mm diameter; (f) with an aperture of 6.5 mm diameter.

4.4.3 Experimental results at 633/1591 nm including artificial turbulence

The experiment done in this section, equals to the one in the previous Section 4.4.2 with the exception of an additional artificial turbulence, which was created via a hair dryer in front of the transmit telescope (cf. Fig. 4.8). The diagrams in Fig. 4.11(a) and (b) show the received optical power versus time at scales of 1.11 μW/mV (1591 nm) and 9.09 μW/mV (633 nm). As one can see, the strong turbulence caused excessive scintillation and fading at the receive telescope up to high frequencies (changed time scale), especially for the small aperture of 6.5 mm diameter. Therefore, the influence of natural turbulence and weather conditions could be neglected. In this experiment, the different behavior of the two wavelengths is clearly observable, but its practical use is limited, because the deep fades appear usually in both wavelength at the same time.

The detail in Fig. 4.11(b) emphasizes an effect, that was observed more often. Special fluctuations of the received power occurred at both wavelength, but displaced in time. One possible explanation of this behavior is given in Fig. 4.11(c). Power measurements of the time-averaged laser beam showed a slight displacement of the two incoming laser spots at the receiver telescope. This may be a result of non-ideal optics due to the large wavelength difference. If additional short term beam wander deflects the whole laser beam, a small receiver aperture can cause the described phenomenon, as suggested in Fig. 4.11(c).

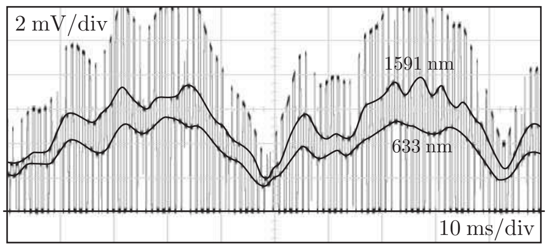

(a) aperture of 15 mm diameter

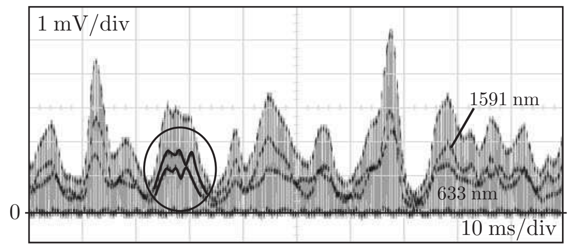

(b) aperture of 6.5 mm diameter

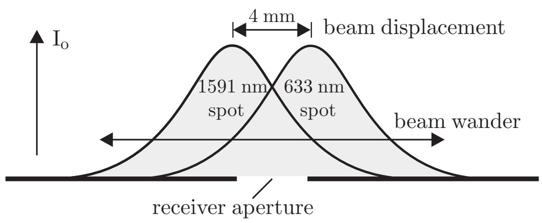

(c) time-averaged received beam

Figure 4.11: Received optical power vs. time at strong artificial turbulence with an aperture of (a) 15 mm and (b) 6.5 mm. Vertical scale: 1.11 μW/mV for 1591 nm and 9.09 μW/mV for 633 nm. (c) The two different wavelengths caused slightly displaced beam spots at the receive telescope.

4.5 Conclusion

The measurements of the previous sections have shown that the wavelength dependency of atmospheric turbulence for moderate wavelength distances in the infrared range is too small for the efficient and practical use of wavelength diversity.

Appendices

Appendix A

Datasheets

A.1 Pin-receiver

Type: R2860C Digital Receiver OC-192/STM-64 from Lucent Technologies.

Absolute Maximum Ratings

Parameter	Symbol	Min	Max	Unit
Operating Temperature Range	T_{OP}	–5	70	°C
Storage Case Temperature Range	Tstg	–40	85	°C
Preamp Supply Voltage	V_{CC}	—	12	V
Photodiode Bias Voltage	V_{PD}	—	20	V
Optical Input Power	P_{IN}	—	4	dBm

Electrical/Optical Characteristics

Table 2. Electrical and Optical Characteristics (25 °C Case Temperature)

Parameter	Symbol	Min	Typ	Max	Unit
Optical Wavelength Range	λ	1280	—	1580	nm
Sensitivity (10^{-10} BER, PRBS 2^{23}-1)	—	—	–20	–18	dBm
Overload (10^{-13} BER, PRBS 2^{23}-1)	—	0	2	—	dBm
Responsivity	R	0.7	0.8	—	A/W
Dark Current	I_D	—	—	1	nA
High-Frequency Cutoff	—	8.0	9.0	—	GHz
Low-Frequency Cutoff	—	—	—	30	kHz
Transimpedance	Z	1400	2000	—	Ω
Maximum ac Output Voltage Swing	—	—	800	—	mVp-p
RF Output Return Loss* (0.1 GHz—5 GHz)	RL_{RF}	—	—	10	dB
Optical Return Loss	ORL	27	—	—	dB
Logic Sense	—	—	Noninverting	—	—
Preamp Supply Voltage	(V_{CC})	7.6	8.0	8.4	V
Photodiode Supply Voltage	V_{PD}	7	8	12	V
Supply Current	I_{CC}	—	80	120	mA

A.2 CWDM multiplexer

BR WAVE CORPORATION

TEST DATA SHEET

Product Description:	8CH CWDM Mux Module
Part Number:	733-47122
Serial Number:	25-1697Z
Date:	10/31/05
Spec. Rev #:	21-050902/A

1. Optical Data

Channel	Temper-ature	IL@CW		Max. In-Band Loss	Adj-Ch Isolation	Non-Adj Ch Isolation	Ripple	TDL (Relative to 23℃)	PDL	RL	Directivity
					≧12.0dB	≧12.0dB	≦0.50dB	≦0.25dB	≦0.10dB	≧45dB	≧50dB
1471	-5℃	≦2.70dB	0.51	0.54	49.7	65.5	0.03	0.02	0.03	54	80
	23℃		0.49	0.51	49.7	67.8	0.03				
	70℃		0.48	0.51	49.6	66.9	0.03				
1491	-5℃	≦2.70dB	0.57	0.70	50.2	68.4	0.16	0.09	0.02	54	71
	23℃		0.56	0.70	50.3	68.4	0.17				
	70℃		0.65	0.78	50.2	68.3	0.16				
1511	-5℃	≦2.70dB	0.98	1.10	47.0	61.7	0.15	0.08	0.02	52	71
	23℃		0.96	1.08	47.0	61.7	0.13				
	70℃		1.04	1.17	47.1	62.5	0.15				
1531	-5℃	≦2.70dB	1.31	1.35	48.0	62.6	0.07	0.06	0.01	51	71
	23℃		1.28	1.31	48.1	63.5	0.06				
	70℃		1.34	1.37	48.1	62.1	0.07				
1551	-5℃	≦2.70dB	2.10	2.21	47.2	63.5	0.11	0.05	0.06	51	71
	23℃		2.05	2.17	47.4	62.8	0.12				
	70℃		2.10	2.24	47.3	63.1	0.14				
1571	-5℃	≦2.70dB	1.44	1.48	45.1	61.5	0.14	0.05	0.02	50	71
	23℃		1.38	1.42	45.3	61.7	0.15				
	70℃		1.43	1.46	45.1	61.3	0.14				
1591	-5℃	≦2.70dB	1.20	1.31	42.9	65.7	0.16	0.11	0.02	50	68
	23℃		1.09	1.18	43.1	65.8	0.14				
	70℃		1.10	1.18	43.0	65.8	0.10				
1611	-5℃	≦2.70dB	2.19	2.26	17.4	14.9	0.12	0.12	0.03	49	71
	23℃		2.07	2.12	17.4	14.8	0.11				
	70℃		2.00	2.04	17.4	14.6	0.09				

RL of Common Port	≧45dB	50

Note : All data are measured with connector

2. Dimension of the protective case and length of pigtails

Pigtail		
All Fiber Length	100±10cm	Pass
Case		
Length	120±0.2mm	Pass
Width	80±0.2mm	Pass
Height	8±0.2mm	Pass

3. Condition of the connectors endface and the case surface

The endface of connectors	Check
1. Contamination Inspection (e.g. dust, oil, fingerprints)	Pass
2. Scratches and Digs Inspection	Pass
3. Geometric Inspection of Endface	Pass

Case	Check
Contamination Inspection (e.g. dust, oil, fingerprints)	Pass

A.3 CWDM demultiplxer

BR WAVE CORPORATION — **TEST DATA SHEET**

Product Description:	8CH CWDM Demux Module
Part Number:	733-47123
Serial Number:	25-1698Z
Date:	10/31/05
Spec. Rev #:	21-050902/A

1. Optical Data

Channel	Temper-ature	IL@CW		Max. In-Band Loss	Adj-Ch Isolation	Non-Adj Ch Isolation	Ripple	TDL (Relative to 23℃)	PDL	RL	Directivity
					≥30.0dB	≥40.0dB	≤ 0.50dB	≤ 0.25dB	≤ 0.10dB	≥45dB	≥60dB
	-5℃		0.46	0.51	45.0	53.5	0.09				
1471	23℃	≤ 3.00dB	0.44	0.50	45.1	53.6	0.09	0.01	0.03	51	80
	70℃		0.43	0.48	45.5	53.8	0.09				
	-5℃		0.57	0.64	47.5	52.4	0.07				
1491	23℃	≤ 3.00dB	0.56	0.63	47.6	52.7	0.07	0.01	0.02	48	75
	70℃		0.57	0.63	47.6	52.6	0.07				
	-5℃		2.16	2.24	57.0	54.4	0.08				
1511	23℃	≤ 3.00dB	2.03	2.12	56.9	54.6	0.09	0.12	0.06	55	60
	70℃		2.06	2.15	56.8	54.5	0.09				
	-5℃		1.95	2.02	47.9	54.8	0.09				
1531	23℃	≤ 3.00dB	1.88	1.93	48.0	55.0	0.08	0.07	0.04	61	75
	70℃		1.84	1.87	48.0	55.0	0.08				
	-5℃		1.09	1.12	46.3	59.4	0.03				
1551	23℃	≤ 3.00dB	0.98	1.01	46.4	60.0	0.03	0.11	0.02	57	75
	70℃		0.92	0.94	46.3	60.2	0.03				
	-5℃		1.57	1.74	45.7	52.9	0.20				
1571	23℃	≤ 3.00dB	1.46	1.63	45.9	53.0	0.20	0.12	0.04	53	60
	70℃		1.55	1.70	46.0	53.0	0.19				
	-5℃		1.85	1.91	53.9	54.2	0.10				
1591	23℃	≤ 3.00dB	1.67	1.74	54.1	54.5	0.10	0.17	0.02	51	60
	70℃		1.64	1.71	54.2	54.7	0.09				
	-5℃		0.86	0.96	48.7	66.3	0.14				
1611	23℃	≤ 3.00dB	0.77	0.86	48.6	66.4	0.14	0.09	0.03	53	75
	70℃		0.79	0.89	48.8	66.3	0.16				

RL of Common Port	≥45dB	51

Note : All data are measured with connector

2. Dimension of the protective case and length of pigtails

Pigtail		
All Fiber Length	100±10cm	Pass
Case		
Length	120±0.2mm	Pass
Width	80±0.2mm	Pass
Height	8±0.2mm	Pass

3. Condition of the connectors endface and the case surface

The endface of connectors	Check
1. Contamination Inspection (e.g. dust, oil, fingerprints)	Pass
2. Scratches and Digs Inspection	Pass
3. Geometric Inspection of Endface	Pass

Case	Check
Contamination Inspection (e.g. dust, oil, fingerprints)	Pass

Abbreviations

List of abbreviations

APC	angled physical contact connector
APD	avalanche photodiode
ATT	attenuation
B2B	back-to-back
BER	bit error ratio
CD	chromatic dispersion
CCD	charge coupled device
CW	continuous wave
CWDM	coarse wavelength division multiplexing
DC	direct current
DCA	digital communication analyzer
DEMUX	demultiplexer
DFB	distributed feedback laser
DFT	discrete fourier transformation
DML	directly modulated laser
DWDM	dense wavelength division multiplexing
EDC	electronic dispersion compensation
EDFA	Erbium doped fiber amplifier
EFEC	enhanced forward error correction
ESD	electro static discharge
FEC	forward error correction
FFT	fast fourier transformation
FM	frequency modulation
FSO	free-space optics
FTTB	fiber to the business
FTTC	fiber to the curb
FTTH	fiber to the home
FWHM	full width at half maximum
GEO	geostationary orbit
HAP	high altitude platform
IC	integrated circuit
IM	intensity modulation
ITU	International Telecommunications Union
LAN	local area network
LOS	line of sight
MUX	multiplexer
NRZ	non-return-to-zero
OSA	optical spectrum analyzer
PON	passive optical network
PRBS	pseudo random bit sequence
RF	radio frequency
RS	Reed Solomon code

RX	receiver
SFEC	standard forward error correction
SONET	synchronous optical network
SSMF	standard single-mode fiber
TFF	thin film filter
TIA	transimpedance amplifier
TX	transmitter
ISI	inter-symbol interference
VCSEL	vertical cavity surface emitting laser
VNA	vectorial network analyzer
WDM	wavelength division multiplexing

Bibliography

[1] K. G. Coffman and A. M. Odlyzko, "Growth of the internet," *Optical Fiber Telecommunications IV B, Academic Press, I. Kaminow and T. Li (ed.)*, pp. 17–57, 2002.

[2] ITU-T, *G.694.2, Spectral grids for WDM applications: CWDM wavelength grid*, International Telecommunication Union, 2002.

[3] ITU-T, *G.694.1, Spectral grids for WDM applications: DWDM frequency grid*, International Telecommunication Union, 2002.

[4] ITU-T, *G.695, Optical interfaces for coarse wavelength division multiplexing applications*, International Telecommunication Union, 2005.

[5] H. Thiele, P. Winzer, J. Sinsky, L. Stulz, L. Nelson, and F. Fidler, "160-Gb/s CWDM capacity upgrade using 2.5-Gb/s rated uncooled directly modulated lasers," *IEEE Photonics Technology Letters*, Vol. 16, no. 10, pp. 2389–2391, 2004.

[6] N. Nishiyama, C. Caneau, J. Downie, M. Sauer, and C. Zah, "10-Gbps 1.3 and 1.55-μm InP-based VCSELs: 85 °C 10-km error-free transmission and room temperature 40-km transmission at 1.55-μm with EDC," in *Proc. of OFC'06, PDP23*, 2006.

[7] P. Winzer, F. Fidler, M. Matthews, L. Nelson, H. Thiele, J. Sinsky, S. Chandrasekhar, M. Winter, D. Castagnozzi, L. Stulz, and L. Buhl, "10-Gb/s upgrade of bidirectional CWDM systems using electronic equalization and FEC," *Journal of Lightwave Technology*, Vol. 23, no. 1, pp. 203–209, 2005.

[8] ITU-T, *G.709, Interfaces for the Optical Transport Network (OTN)*, International Telecommunication Union, 2003.

[9] ITU-T, *G.975, Forward error correction for submarine systems*, International Telecommunication Union, 2000.

[10] Applied Micro Circuits Corporation (AMCC). (2006) DispersionXX-2 chipset. [Online]. Available: www.amcc.com

[11] Vertilas. (2006) Technology for long wavelength VCSELs. [Online]. Available: www.vertilas.com/pdf/Optical_technologies.pdf

[12] OFS Optics. (2006) AllWave fiber, datasheet. [Online]. Available: www.ofsoptics.com

[13] Corning. (2006) SMF28-e fiber, datasheet. [Online]. Available: www.corning.com

[14] W. Leeb, *Photonik und optische Nachrichtentechnik Vertiefung, Script VO 389.084*, Institute of Communication and Radio-Frequency Engineering, Vienna University of Technology, 2005.

[15] Browave Corporation. (2006) 8-channel CWDM multiplexer, specifications. [Online]. Available: www.browave.com

[16] Hamamatsu. (2006) G10204/G9284 APD/pin-receiver, datasheet. [Online]. Available: www.sales.hamamatsu.com/en/products/solid-state-division/optical-communication-devices/high-speed.php

[17] Northlight Optronics. (2006) 10Gbps APD/pin-receiver, datasheet. [Online]. Available: www.northlightoptronics.com

[18] CyOptics. (2006) 10Gbps APD/pin-receiver, datasheet. [Online]. Available: www.cyoptics.com/dynContentFolder/1640_41.pdf

[19] P. J. Corvini and T. L. Koch, "Computer simulation of high-bit-rate optical fiber transmission using single-frequency lasers," *Journal of Lightwave Technology*, Vol. 5, no. 11, pp. 1591–1595, 1987.

[20] F. Fidler, "Performance enhancement in WDM-systems," Diploma thesis, Institute of Communication and Radio-Frequency Engineering, Vienna University of Technology, 2004.

[21] M. Pfennigbauer, "Design of optical space-to-ground links for the International Space Station," Doctoral thesis, Institute of Communication and Radio-Frequency Engineering, Vienna University of Technology, 2004.

[22] B. Eichinger, "Atmospheric impact on a terrestrial laser-link system and its compensation," Diploma thesis, Institute of Communication and Radio-Frequency Engineering, Vienna University of Technology, 2006.

[23] R. J. Sasiela, *Electromagnetic wave propagation in turbulence.* Berlin: Springer-Verlag, 1994.

[24] R. Purvinskis, D. Giggenbach, H. Henniger, N. Perlot, and F. David, "Multiple wavelength free-space laser communications," in *Proc. of SPIE, Free-Space Laser Communication Technologies XV*, Vol. 4975, 2003, pp. 12–19.